



DEPARTMENT OF PHYSICS

TECHNICAL UNIVERSITY MUNICH

Bachelor of Science (B.Sc.)

**Development of a LIDAR System for
Characterizing the Optical Properties of
Seawater at Cascadia Basin**

Author: Christopher Fink
Professor: Prof. Elisa Resconi
Supervisor: Dr. Christian Fruck
Submission Date: August 26, 2019



Christopher Fink: *Development of a LIDAR System for Characterizing the Optical Properties of Seawater at Cascadia Basin*, © August 26, 2019

ABSTRACT

Using neutrinos as messengers for astronomical observations is a relatively new field and has so far only lead to a single marginal detection of an astrophysical object[19]. Nevertheless, several instruments for neutrino astronomy have been built over the past decade or are still under construction. Ice-Cube [Referenz suchen], installed at the South Pole, about 2km deep inside the glacier, is the most advanced and most successful project to date. Several other projects, among them Antares [ref.], KM₃Net [ref.] and GVD [ref.], are attempting to go deep under water instead of into ice. This has the advantage of an easier and more precise reconstruction of neutrino events, due to less scattering when compared to ice.

STRings for Absorption length in Water b (STRAW-b) and its predecessor STRAW are experiments located at Cascadia Basin in the pacific ocean next to Vancouver Island in a depth of 2600 m b s l. Its goals are the characterisation of the optical properties of the seawater, namely the attenuation length, and the background light, coming from the ⁴⁰K decay and the bioluminescence. An instrument for STRAWb is the **L**ight **D**etection **A**nd **R**anging (LIDAR). Its purpose is to give independent measurements of the attenuation and the backscatter coefficient.

In the course of this thesis, we developed a new design for the LIDAR optics to suite the limited space inside the glass sphere and the small size of the used μ PMT. The light emitter is a nanosecond pulsed laser with a central wavelength of 450 nm. the design of the optical system was based on simulations done with the pyOpTools-package for Python and was later cross-checked with a more sophisticated simulation in geant4. To complement this a simulation of the return signal has been written implemented in order to be able to adapt the readadout electronics and plan the data analysis. In addition, a few first measurements have been performed to check whether the designed optics worked as simulated or not.

CONTENTS

I	PHYSICAL INTRODUCTION	1
1	NEUTRINO-PHYSICS	2
1.1	The Standardmodel	2
1.2	Origins of Neutrinos	2
1.2.1	Solar Neutrinos	2
1.2.2	Supernova Neutrinos	3
1.2.3	Atmospheric Neutrinos	3
1.3	Neutrino Interactions	4
1.3.1	Cherenkov Effect	5
1.4	Neutrino Telescopes	5
1.4.1	IceCube	6
1.4.2	STRAW	6
1.4.3	STRAW-b	7
1.5	Optical Properties of Water	8
II	THE LIDAR-SYSTEM	10
2	LIDAR	11
2.1	Principle of the LIDAR-Systems	11
2.2	LIDAR-Equation	12
2.3	Different LIDAR Techniques	12
2.3.1	Elastic Backscatter LIDAR	12
2.3.2	Raman LIDAR	13
2.3.3	Differential Absorption LIDAR (DIAL)	13
2.3.4	Other LIDAR Techniques	13
3	EXPERIMENTAL SETUP	14
3.1	The Laser	14
3.2	The μ PMT	15
3.3	The Optics	17
III	SIMULATION AND RESULTS	22
4	SIMULATION	23
4.1	Simulation of the LIDAR Geometry using pyOpTools	23
4.1.1	The PyOpTools Package	23
4.1.2	Position of the LIDAR parts	24
4.1.3	Ideal laserposition	26
4.1.4	Maximal possible offset	27
4.1.5	verification only in Air	30
4.2	Simulation of the LIDAR Geometry using geant4	31
4.2.1	Setup	31
4.2.2	Position of the LIDAR parts	34
4.2.3	Ideal Laserposition	35

4.2.4	Maximal possible offset	37
4.2.5	Verification only in Air	39
4.3	Comparison of the simulations	40
4.4	Simulation of the Return Signal	40
5	RESULTS	43
5.1	Opening Angle of the Laser	43
5.2	First Measurements	44
5.2.1	c_0 Validation	44
5.2.2	First LIDAR Measurement	45
5.3	Conclusion and Foresight	46
IV	APPENDIX	47
A	PYTHON CODE	48
	BIBLIOGRAPHY	52

LIST OF FIGURES

Figure 1	Schematic view of a cosmic ray air shower[13]	4
Figure 2	Technical drawings of STRAW and STRAWb provided by Christian Spannfellner and Kilian Holzapfel	8
Figure 3	The figure shows the general principle of the LIDAR	11
Figure 4	Image of the different pulse width of the laser. Data provided via Thorlabs[24]	14
Figure 5	Images of the laser with and without its housing and already mounted on the final LIDAR	15
Figure 6	Image of the working principle of the μ PMT as provided by Hamamatsu[16]	15
Figure 7	wavelength dependant count sensitivity of the μ PMT [16]	16
Figure 8	Dark count measured by Hamamatsu[16]	16
Figure 9	Images of the first housing version.	17
Figure 10	Comparison of a normal filter to the premium filter I use. Red is the premium filter.[22]	18
Figure 11	Images of the final housing version	19
Figure 12	Front view one the housing of the μ PMT and inside a simplified version of the μ PMT	20
Figure 13	Images of the final LIDAR	21
Figure 14	This picture was taken from the simulation. The cyan coloured lens represents the water, the big yellow one the glass sphere surrounding the module, the red one the filter and the small lens is the focusing lens. The returned light rays were made by the latter method described in the section	24
Figure 15	The detected spot size with 64 mm distance between detector and the centre of the lens	25
Figure 16	Same setup as in figure 15 but with ± 1 mm difference to the ideal position	25
Figure 17	Image of what a detector at 149 m distance to the LIDAR would see. The big spots are marking the corner of the field-of-view of the detector and the small one the laser beam.	26
Figure 18	The detected spot size with 64 mm distance between detector and the centre of the lens and a maximum offset for the laser described before	27
Figure 19	The laser is in the ideal position described above and with a varying offset of ± 20 mm difference.	28

Figure 20	The laser beam with the offset described above and with a varying distance along the z-axis of ± 20 mm from the ideal position.	28
Figure 21	The laser beam with the offset described above and with a varying offsets in the x- and y-direction	29
Figure 22	Side view and the detected spot for a distance of 59.05 mm from the middle of the lens.	30
Figure 23	Two Images of the LIDAR-Setup in the Geant4 Simulation. Black Area represents the Water, the darker grey the Sphere and the lighter grey area inside the Air, in Yellow the lens and the filter, in Cyan the detector and the white area around the filter a (not existing in the real module) ring in order to absorb any rays that would miss the detector.	32
Figure 24	The detected spot size with 64 mm distance between detector and the centre of the lens. The green circle marks the area where 68.3 % of the detected photons are included and the blue circle the area with 95.5 %. This will be the case for all following figures.	34
Figure 25	Same setup as in figure 24 but with ± 1 mm difference to the ideal position	34
Figure 26	An Image of what a detector at 149 m distance to the LIDAR would see.	36
Figure 27	A detailed and a view with the detector for comparison of the detected spot size with 64 mm distance between detector and the centre of the lens and a maximum offset for the laser described before.	37
Figure 28	The laser is in the ideal position and with a varying offset of ± 20 mm difference.	37
Figure 29	The laser beam with the offset described above and with a varying distance along the z-axis of ± 20 mm from the ideal position. The red box marks the edge of the detector.	38
Figure 30	The laser beam with the offset described above and with a varying offsets in the x- and y-direction	38
Figure 31	Side by side comparison of the best spot and where the best spot should be.	39
Figure 32	Range corrected return signal for 1 s of observation with the described settings.	41
Figure 33	Range corrected return signal for 60 s of observation with the described settings.	42
Figure 34	Measured diameters of the laser beam in x- and y-direction	44
Figure 35	time delay between the shot of the beam and the detection of the backscattered light	45
Figure 36	The expected amount of photons per trigger for various distances fitted with a r^{-2} function.	46

LIST OF TABLES

Table 1	Thorlabs lens information	18
Table 2	For the three simulated distances their centre and the diameter of a circle, which contains 90 % of the detected photons	35

ACRONYMS

LIDAR **L**ight **D**etection **A**nd **R**anging

pyOpTools A python package which enables simulations for optical systems via raytracing

PMT PhotoMultiplier Tube

geant4 **G**eometry **a**nd **T**racking; A Monte Carlo Simulation developed at Cern for accurately simulating particle physics; Written in C++

STRAW **S**TRings for **A**bsorption length in **W**ater, Our first Pathfinder experiment for a future neutrino telescope

STRAW-b **S**TRings for **A**bsorption length in **W**ater **b**, Our extension for STRAW. Dedicated for characterizing the background and independent measurements of the attenuation coefficient.

P-ONE Pacific Ocean Neutrino Explorer

POCAM Precision Optical Calibration Module

DOM Digital Optical Module

SDOM STRAW Digital Optical Module

Part I

PHYSICAL INTRODUCTION

This part will focus on the neutrino physics and it will give a short introduction into neutrino telescopes. After that we will go more into detail about the optical properties of seawater.



NEUTRINO-PHYSICS

1.1 THE STANDARD MODEL

The Standard Model of particle physics is, at this time, the best theoretical model that describes our universe on a fundamental level. It consists of the three fermion generations and the five gauge bosons which are mediating the strong, weak and electromagnetic forces. The only fundamental force which is not yet included in the gravitational force. The latest discovery was the Higgs Boson. The LHC discovered it in 2012, which proved the "Higgs Mechanism", postulated in 1964, which is responsible for generating the mass of the particles[5].

Each of the three generations of the fermions consists of a quark and a lepton pair. In contrast to the quark pairs, which are all electrically charged, only half of the lepton pairs are charged, namely the e^\pm , μ^\pm and the τ^\pm . Their corresponding partners, the neutrinos (ν_e, ν_μ, ν_τ) are neither carrying colour nor charge and are thus only interacting via the weak interaction

1.2 ORIGINS OF NEUTRINOS

As neutrinos are only interacting weakly, they can travel almost undisturbed from their source to use and therefore give us the possibility to observe processes that would be inaccessible otherwise. In the following, we will go more into detail about the various known and predicted sources of neutrino emission. These origins can either be artificial, e. g. from β decays in fission reactors, nuclear bombs or accelerators and reaching energies up to a few MeV[2]. Alternatively, they can be of natural origin. A few of these origins will be outlined in the following paragraphs.

1.2.1 SOLAR NEUTRINOS

Our sun is the best known astrophysical neutrino source with the largest extraterrestrial neutrino flux[3]. The first observation of a neutrino flux was in 1970 by the Homestake Experiment[11] and then later followed by various other neutrino detector, e. g. Kamiokande or GALLEX.

Every active star, like our sun, produces its energy by fusing lighter particles

into heavier ones. For most of its lifetime this is done in the pp-chain[20]. The process can be written as:



This produces neutrinos up to energies of 14 MeV[15]. The discovery of the solar neutrino flux led to the famous *solar neutrino problem*. This problem is the large discrepancy between the predicted neutrino flux and the measured. Only around 1/3 of the predicted flux was measured. It was not resolved until 2001 when the Sudbury Neutrino Observatory found evidence for a *flavor oscillation*[9].

Since neutrinos interact weakly, they can be identified with a flavor eigenstate. However, these eigenstates are not identical with their mass eigenstates. They are a compositions of all the flavor eigenstates. This mixing is described in the the PMNS-Matrix. Neutrino oscillation describes the process in which the flavor of a neutrino oscillates into another while propagating through space.

1.2.2 SUPERNOVA NEUTRINOS

At the end of a stars lifetime, when it has fused the majority its elements, the radiation pressure begins to shrink, and due to gravity, the core starts to collapse under its own weight. This collapse is followed by a rapid explosion with an extremely high energy release. In this process, massive amounts of neutrinos get produced in a short time. For type II supernovae, 99% of liberated gravitational binding energy is estimated to be carried away by neutrinos.[15]. Although many supernovae have been detected, the only one of which a clear neutrino flux measured is *SN1987A*. On February 2nd, 1987 the three neutrino detectors Kamiokande II, IMB and Baksan detected a neutrino burst that lasted around 12 s. Around three hours after that the visible light from that supernova reached the earth.

1.2.3 ATMOSPHERIC NEUTRINOS

Atmospheric neutrinos are the result of the interaction of charged hadrons, called *cosmic rays*, with nuclei in the earths atmosphere, typically around 15 km above the earths surface. These cosmic rays consists primarily of protons. For high energetic cosmic rays these interactions are deeply inelastic. Therefore the produced Pions and, less abundantly, Kaons are forward peaked. The charged pions (and analogous the Kaons) then decay via a semileptonic process mainly into muons and muon-neutrinos:

$$\pi^+ \rightarrow \mu^+ + \nu_\mu \quad (1.2.2)$$

$$\pi^- \rightarrow \mu^- + \bar{\nu}_\mu \quad (1.2.3)$$

If the muon decays before hitting the ground, it produces electrons and electron-neutrinos through the same weak process:

$$\mu^+ \rightarrow e^+ + \nu_e + \bar{\nu}_\mu \quad (1.2.4)$$

$$\mu^- \rightarrow e^- + \bar{\nu}_e + \nu_\mu \quad (1.2.5)$$

The spectrum of this process generally peaks in the GeV range[15]. Figure 1 shows an illustration of such a cosmic ray induced air shower:

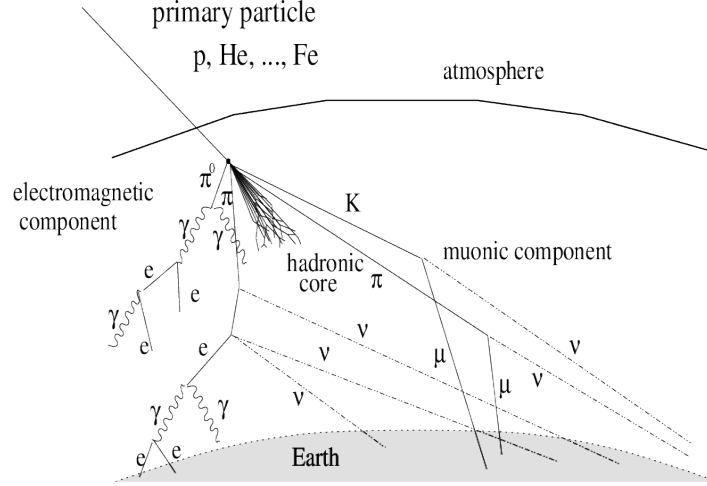


Figure 1: Schematic view of a cosmic ray air shower[13]

For low energies ($E \lesssim 1 \text{ GeV}$) most of the muons decay before they hit the ground. Therefore the neutrino fluxes are expected to satisfy the following ratios:

$$\frac{\phi_{\nu_\mu} + \phi_{\bar{\nu}_\mu}}{\phi_{\nu_e} + \phi_{\bar{\nu}_e}} \simeq 2, \quad \frac{\phi_{\nu_\mu}}{\phi_{\bar{\nu}_\mu}} \simeq 1 \quad (1.2.6)$$

This ratio could not be verified in the Super-Kamiokande detector and the Sudbury Neutrino Observatory. This anomaly was again solved through neutrino oscillations.

1.3 NEUTRINO INTERACTIONS

When a high-energy neutrino travels through matter, it can interact either via a charged current (CC) weak interaction or a neutral current (NC) weak interaction. The generalized interactions are:

$$\nu_l + N \rightarrow l + X \quad (\text{CC}) \quad (1.3.1)$$

$$\nu_l + N \rightarrow \nu_l + X \quad (\text{NC}) \quad (1.3.2)$$

N being a nuclei, X the produced hadron and $l = \{e, \mu, \tau\}$.

Neutral current events gives the same signature for all neutrino flavors. For these events a significant part of the energy is carried away by the initial neutrino and thus stays unobserved. This increases the error on the reconstructed

energy of the primary neutrino. On the other hand for charged current events the opposite is the case. Most of the energy will be transferred in the produced lepton [6].

Due to the large amount of energy transferred to the secondary particles, various processes are available to them. At high energies the *Cherenkov Effect* will be the significant contribution to the photon production. Most of the neutrino detectors use this effect for a detecting neutrinos. This is also the main reason why transparent media like ice or water are used.

1.3.1 CHERENKOV EFFECT

If a particle's energy is sufficiently high, it can travel faster than the speed of light in a medium. For a dielectric medium with a refractive index n the speed of light in this medium is given by:

$$c_n = \frac{c_0}{n} \quad (1.3.3)$$

When the charged particle moves through this medium, it will polarize the molecules locally along its track. As long as the velocity of the particle is $v \leq c_n$ than the local polarization will annihilate. However, when the particle moves with a velocity greater than the speed of light in this medium, an overall dipole moment will build up which relaxes back to equilibrium through radiation. This coherent radiation is emitted in a cone with a characteristic angle θ_c . It is given by:

$$\cos\theta_c = \frac{1}{\beta n} \quad (1.3.4)$$

n is again the refractive index of the medium and $\beta = v/c$ is the ratio of the particle velocity and the speed of light. For highly relativistic particles in sea water the Cherenkov angle is $\beta_c \lesssim 43^\circ$. [6]

The number of emitted Cherenkov photons N_γ per wavelength $d\lambda$ and per unit traveled dx by a particle with the charge $q = z \cdot e$ is given by the equation:

$$\frac{d^2N}{dx d\lambda} = \frac{2\pi\alpha z^2}{\lambda^2} \left(1 - \frac{1}{n(\lambda)^2 \beta^2}\right) \quad (1.3.5)$$

This equation shows that smaller wavelengths contribute more significantly to the Cherenkov radiation. For water and ice is the typical light output in the visible range between 300 - 600 nm. [6]

1.4 NEUTRINO TELESCOPES

As already mentioned, neutrinos only interact via the weak force. On the one hand that has advantages, e.g. that neutrinos leave supernovae unhindered, on the other hand this means they are tough to detect. The basic idea that all currently operating neutrino telescopes have in common, is using light detectors (e.g. PMTs) inside a transparent medium like deep ice or water filling a

huge volume in order to detect the described Cherenkov radiation. Due to the rare interactions they need to be usually build around the cubic kilometer scale to be sensitive enough. In the following will be the most successful neutrino telescope, IceCube, alongside the pathfinder missions STRAW and STRAW-b briefly described.

1.4.1 ICECUBE

The IceCube Neutrino detector is located at the South Pole and is operating since 2010. It consists of 5160 optical sensors attached to 86 strings in total between 1450 m and 2450 m. These sensors are referred to as Digital Optical Modules (DOMs). Each of these DOMs consists of a 10" PhotoMultiplier Tube (PMT), which faces downwards. Together with the read-out electronics, it is packed in a 330 mm glass sphere. 78 of these strings are forming the primary in-ice array with a vertical separation of 17 m between the DOMs and a spacial extension of about one cubic kilometer. This design meet the requirements for detecting astrophysical neutrinos in the range of 10^3 GeV to 10^6 GeV [8]. Additionally, a subarray called DeepCore was deployed. It consists of the missing eight closely-spaced strings. This spacing is on average 72 m. It is optimized for low-energy events in the range of 10 GeV to 100 GeV.

Unlike normal ice, glacial ice at a depth of more than 1300 m gets transparent in the range of visible light. Its peak is at around 2400 m with a average scattering length of 50 m and an average absorption length of 190 m[10].

In 2017, IceCube was able to associate a Neutrino event with a neutrino point-source, the blaser TXS 0506+56[19]. This evidence was further supported by a burst of neutrino events of the year 2015 that also coincided with flaring activity of the source in gamma rays and other wavelength bands[7].

1.4.2 STRAW

"STRings for Absorption length in Water" (STRAW) is a pathfinder mission towards a future neutrino detector named Pacific Ocean Neutrino Explorer (P-ONE). Its main task is to characterize the Cascadia Basin site at the west coast of Canada in the pacific ocean by measuring the attenuation and scattering length in the range of 350 nm and 600 nm alongside the overall ambient background induced by ^{40}K and bioluminescent light. It consists of 2 strings each of them 115 m long and 37 m apart and both located approximately 2600 m b.s.l. On the strings are five SDOMs and three POCAMs mounted (See figure 2a for details). The Precision Optical Calibration Modules (POCAMs) emit isotropic light flashes on a nanosecond scale in various wavelengths. These flashes get detected with a 3" PMT inside the STRAW Digital Optical Modules (SDOMs) and therefore gives access to the properties of the seawater[4].

1.4.3 STRAW-B

STRAW-b is an addition to STRAW. Its main goals are on the one hand to provide more in-depth measurements of the bioluminescence and additional independent measurements for the the attenuation length of the sea water and on the other hand to develop a deployment strategy for a large scale neutrino telescope. In contrast to STRAW, STRAW-b consists only of one single string which is 430 m long. It will consist of five standard modules and five specialized modules. Each of the modules are 24 m apart from each other. (For details see figure 2b) Those specialised modules will be three PMT-Spectrometers, a Muon Tracker, and the LIDAR which is the topic of this thesis. The PMT Spectrometers will investigate the bioluminescence in greater detail. The Muon Tracker will be first device capable of measuring muon tracks and the LIDAR will be used for complementary measurements for the attenuation length and the scattering coefficient. STRAWb is planned to be deployed at the beginning of 2020.

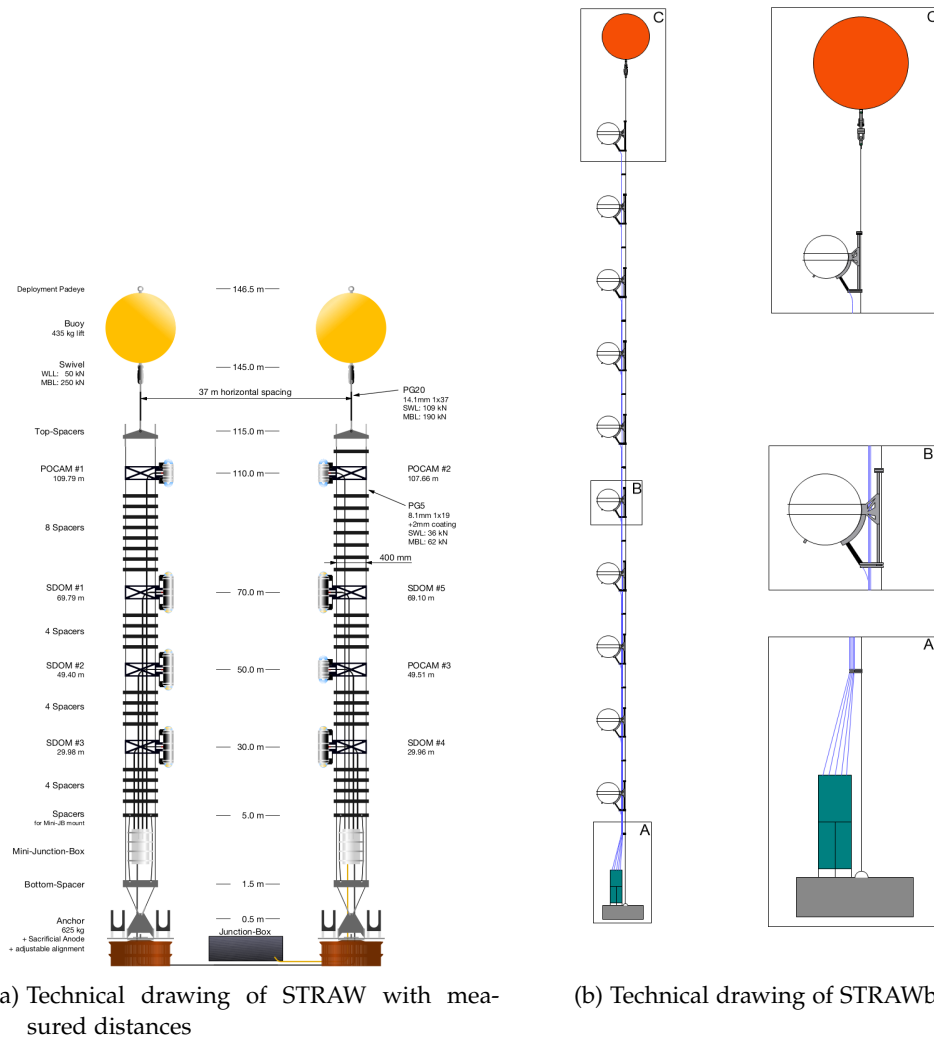


Figure 2: Technical drawings of STRAW and STRAWb provided by Christian Spann-fellner and Kilian Holzapfel

1.5 OPTICAL PROPERTIES OF WATER

As already mentioned in section 1.3 the properties of optical water is a crucial factor for the detection the Cherenkov light. The important properties are scattering and absorption. Absorption reduces the total amount of light on the PMTs and scattering changes the direction of the emitted Cherenkov Photons as well as the distribution of their arrival times on the PMTs. This increases the uncertainties when reconstructing the direction of the incoming neutrino. We can define these properties as followed. The absorption, scattering and attenuation coefficients are:

$$a(\lambda), \quad b(\lambda), \quad \alpha(\lambda) = a(\lambda) + b(\lambda) \tag{1.5.1}$$

These coefficients are all in units of $[m^{-1}]$. Alternatively these properties can also be defined as the absorption, scattering and attenuation length in units of $[m]$:

$$L_a(\lambda) = a(\lambda)^{-1}, \quad L_b(\lambda) = b(\lambda)^{-1}, \quad L_\alpha(\lambda) = \alpha(\lambda)^{-1} \quad (1.5.2)$$

These lengths are defined as the distance the light travels in which its initial intensity I_0 got reduced by a factor of $1/e$ through either of these processes. A general description for scattering at spherical, transparent objects was first done by Gustav Mie in 1908 [18]. In general, when light travels through a transparent medium like water, it can scatter multiple times before entering the detector. The average cosine that has undergone n -times scattering can be described with the following equation:

$$\langle \cos\theta \rangle_n = \langle \cos\theta \rangle^n \quad (1.5.3)$$

This means if $\langle \cos\theta \rangle > 0$ forward scattering is preferred (vice versa if $\langle \cos\theta \rangle < 0$) and if $\langle \cos\theta \rangle = 0$, the scattering has a forward-backward symmetry. Therefore we can define an *effective* scattering length $L_b^{eff}(\lambda)$. It is the length a photon has travelled after n scattering events:

$$L_b^{eff}(\lambda) = L_b(\lambda) \sum_{i=0}^n \langle \cos\theta \rangle^i \simeq \frac{L_b(\lambda)}{1 - \langle \cos\theta \rangle} \quad (1.5.4)$$

These properties depend on various factors. For water those are for example temperature or salinity an essential factor which influences its properties. On the other hand, other chemicals, bacteria or other microorganisms are further scattering centres, which can affect the properties of the seawater. All those properties can be subject to seasonal variations. E. g. the biological activity of microorganisms is known to increase in the spring. Currently, due to a lack of actual measurements, assumptions had to be made for the simulations, which will be described later [6].

Secondly, the optical background of the water plays a significant role when setting up a trigger system for a future detector. This background has two main contributions: the decay of radioactive elements (mostly ^{40}K) and bioluminescence. However, the energy of most of the photons produced in the ^{40}K decay is higher than the Cherenkov light and therefore at least for the LIDAR not relevant [6]. This is not the case for bioluminescence. An analysing image taken during deployment gave rise to the suspicion that Pyrosomes play a key role in the emission of background light recorded with STRAW. This does not mean that other biological sources of light can be excluded. As already mentioned, one of the goals of STRAW-b is to further analyse the spectrum emitted by these creatures.

Part II

THE LIDAR-SYSTEM

The first part will give, in the beginning, an overview over LIDAR-physics on general and will give a few examples of different LIDAR applications. After that the developed LIDAR system for STRAWb will be described.

LIDAR

LIDAR is an acronym and stands for **L**ight **D**etection **A**nd **R**anging. It is a possibility, to retrieve inherent information about an optical medium, namely the back-scattering coefficient and the absorption length.

LIDAR works similarly to the RADAR but uses short-pulsed laser light of the visible spectrum or infrared instead of radio waves. In the first part of this section, the functionality and the principle of a LIDAR will be described, and after that, the parts that were built and used for this thesis.

2.1 PRINCIPLE OF THE LIDAR-SYSTEMS

A LIDAR-system consists mainly of two devices. A short-pulsed Laser and a fast receiver are both aligned. See figure 3 for Details. In the most used case of atmospheric research, those are mirror telescopes collecting the backscattered light. However, due to the different goal of this setup and the limited space, a more telescope-like configuration had been chosen. After that usually, the light gets filtered by wavelength, or polarisation state if needed, to ensure that only the specific wavelength emitted by the laser gets detected. The light will then be detected converted into an electrical signal and amplified. The detailed LIDAR-setup used in this case will be described in the following chapters.[28, pp. 1-18]

The light arrives at different times relative to when the laser was fired. From this time difference, one can calculate the distance at which the scattering took place and therefore gets information about the density of the scattering particles in the medium.

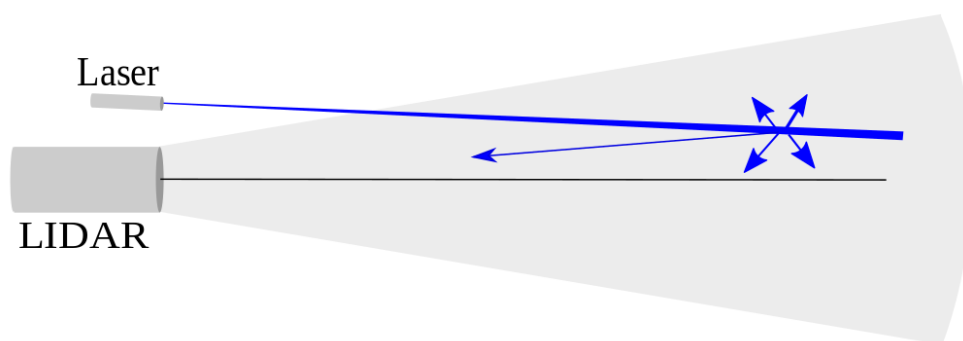


Figure 3: The figure shows the general principle of the LIDAR

2.2 LIDAR-EQUATION

The LIDAR equation for a monochromatic laser can be written in the following form:

$$dN(r) = N_0 C G(r) \frac{A}{r^2} \beta_{\pi}(r) dr \exp\left[-2 \int_0^r \alpha(r') dr'\right] \quad (2.2.1)$$

In this case, it is written in the differential form in which $dN(r)$ describes the differential number of photons counted in the detector with an effective area A and in an interval of dr . C is the overall efficiency of the detector, N_0 the initial amount of photons emitted by the laser and $G(r)$ a function that characterises the overlap between the field-of-view of the receiver and the laser beam. The factor 2 in the exponential function takes the two-way path from the light into account, and the $\alpha(r)$ is the attenuation coefficient at a distant r relative to the position of the LIDAR. This equation generally holds, but for simplicity reasons, a non-distance-dependent attenuation coefficient $\alpha(r) \equiv \alpha$ will be assumed as it is expected at first order in deep ocean water. Therefore the integral in 2.2.1 simplifies to $\alpha \cdot r$.

2.3 DIFFERENT LIDAR TECHNIQUES

Over the years, different LIDAR techniques were developed to serve different tasks (e. g. distance measurements, retrieving optical parameters, etc.). In the following, a few of the most popular (including the one that was used for this experiment) are described.

2.3.1 ELASTIC BACKSCATTER LIDAR

It is the classic and simplest form of a LIDAR and was described in 2.1. It is also the type used in this experiment. A single Laser shoots a short-pulsed beam parallel to the telescope, and the elastically backscattered photons get detected. Where "elastic scattering" means that the wavelength of the scattered electron does not change. With this type of LIDAR, the most straightforward information to obtain is the position and distance of objects which scatters more light relative to the surrounding medium(i. e. clouds in the atmosphere [28, p. 12]). The following equation defines this distance:

$$r_{\text{obj}} = \frac{1}{2} c \Delta t \quad (2.3.1)$$

It is also called "Rayleigh-Mie-LIDAR" because the predominant effects are "Rayleigh Scattering" and "Mie Scattering".

But because our goal is to retrieve information about the backscattering and the attenuation coefficient of the deep sea water, the whole signal will be used and evaluated according to 2.2.1.[14]

2.3.2 RAMAN LIDAR

The Raman LIDAR uses inelastic scattering of the emitted light with the atmospheric molecules. Like the LIDAR described in the section above, it uses a single wavelength laser as well but detects light also at different wavelengths. This is necessary because due to the inelastic scattering, the scattered light lost (or received) energy from the molecules. Those molecules are changing their vibration- and rotation-state in the course of the process. However, a significant drawback is that it happens less frequently ($10^{-4} - 10^{-3}$ times) than the usual Rayleigh scattering. Therefore a strong light source needs to be used to use this technique efficiently. It is especially useful when investigating water-vapour concentration. Different atmospheric gases, like CO_2 , SO_2 or CH_4 , have also been tried to measure. However, routine atmospheric monitoring is hard to achieve due to the necessary detection limits.[28, pp. 241-242]

2.3.3 DIFFERENTIAL ABSORPTION LIDAR (DIAL)

This LIDAR type uses two wavelengths. The first wavelength is chosen in a way, that it has a peak in the absorption spectrum of the gas of interest and the second wavelength in a region of less absorption but as close as possible to the first one in order to guarantee that the behaviour in the rest of the atmosphere is similar. Moreover, since λ_1 and λ_2 are close to each other, their backscattering and extinction coefficients will be roughly the same except in the region where the gas is present. So by comparing the profiles of the returned signal, one can extract information about the gas density profile. This technique is used to measure the profiles of O_3 , NO_2 , SO_2 or H_2O in the atmosphere. [12]

2.3.4 OTHER LIDAR TECHNIQUES

Those three LIDAR types are by far not the only ones existing. There is the **Fluorescence LIDAR** which makes use of the fluorescence of specific atoms and molecules. The **High Spectral Resolution LIDAR (HSRL)** takes advantage of the spectral distribution of the return signal in order to distinguish between aerosol and molecular signals and the **Doppler LIDAR** uses the Doppler shift in order to analyse the velocity of fluids or air.

EXPERIMENTAL SETUP

As already mentioned in section 1.4.3, the whole lidar module consists of more pieces than the actual LIDAR itself. In this chapter, only the parts of the LIDAR will be described. It is composed of 3 major parts: the nanosecond pulsed laser, the μ PMT and the focusing optics. The laser and the μ PMT were both bought of the shelf, but the focusing optic was designed and build based on the results of the pyOpTools simulation. In the following section, we will go more into detail on these three components. However, optics and their design was one of the main parts of this thesis.

3.1 THE LASER

The first major part is the laser. We decided to use the "NPL45B" from Thorlabs. All the following data and images are directly taken from the data sheet provided by Thorlabs[24]. It is a nanosecond pulsed diode laser with a central wavelength of 450(10) nm and a pulse width of 5(1) ns to 39(3) ns. It has a internal trigger for a frequency of 1 MHz, 5 MHz or 10 MHz but is has also a user-triggered mode which allows custom frequencies up to 10 MHz. In figure 4 one can see plots of the different pulse widths:

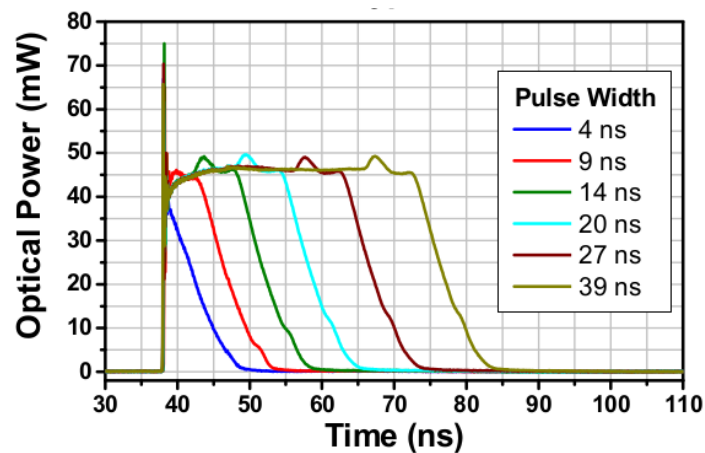
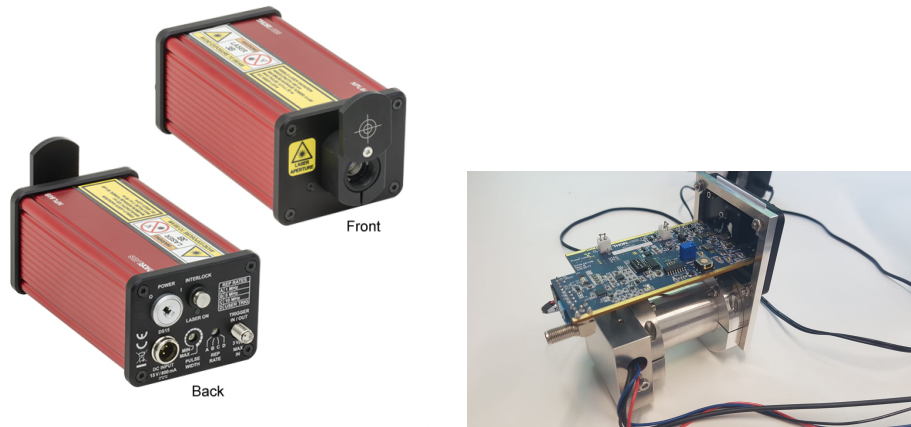


Figure 4: Image of the different pulse width of the laser. Data provided via Thorlabs[24]

In image 5a, we can see the laser as Thorlabs sells it. However, since we are very limited in space and weight for the module, we decided to remove the red aluminium housing. Therefore the controller needed to be reprogrammed that it accepts wider temperature fluctuations because the red housing itself is part of the temperature control.



(a) Image of the laser build and sold from Thorlabs. Picture taken directly from their website[25] (b) The same laser but with the removed housing.

Figure 5: Images of the laser with and without its housing and already mounted on the final LIDAR

The characterization of the opening angle of the laser is described in section 5.1. We determined an approximate opening angle of $\phi = 0.01^\circ$.

3.2 THE μ PMT

For detecting the back-scattered light, we decided to use a "H12406" μ PMT photon counting head from Hamamatsu[16]. It is still larger in dimension than a SiPM, but due to initial problems with the readout of the SiPM and the dark noise rate which is higher by orders of magnitude, we decided to go for the μ PMT instead. But compared to other PMTs, this one is still relatively small with $30 \times 38 \times 15$ mm ($l \times w \times h$). The working principle is the same as for conventional PMTs, and thus performance characteristics are the same. Light hits the Photocathode which emits an electron via the photoelectric effect. This electron gets multiplied in Electron Multipliers (Dynodes) and transferred to the anode. Image 6 shows the working principle of the μ PMT we use:

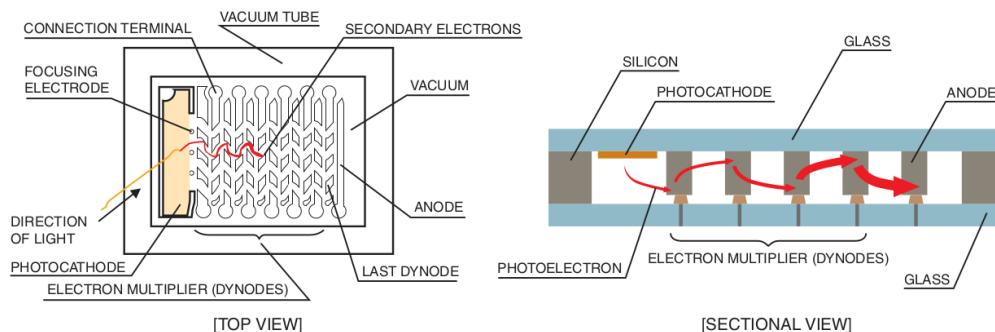


Figure 6: Image of the working principle of the μ PMT as provided by Hamamatsu[16]

The Photocathode consists of Bialkali and operates in the range of 300 nm to 650 nm, and it has an effective area of 1 mm by 3 mm. The last point is also the major drawback of this detector. A width of 1 mm means that the light needs to be focused as much as possible. Minimal errors in the installation of the detector would mean that we would not detect the backscattered photons anymore.

It has a count linearity up to 5×10^6 Hz. This is the value at which 10% of the counted photons get lost compared to the theoretical value.

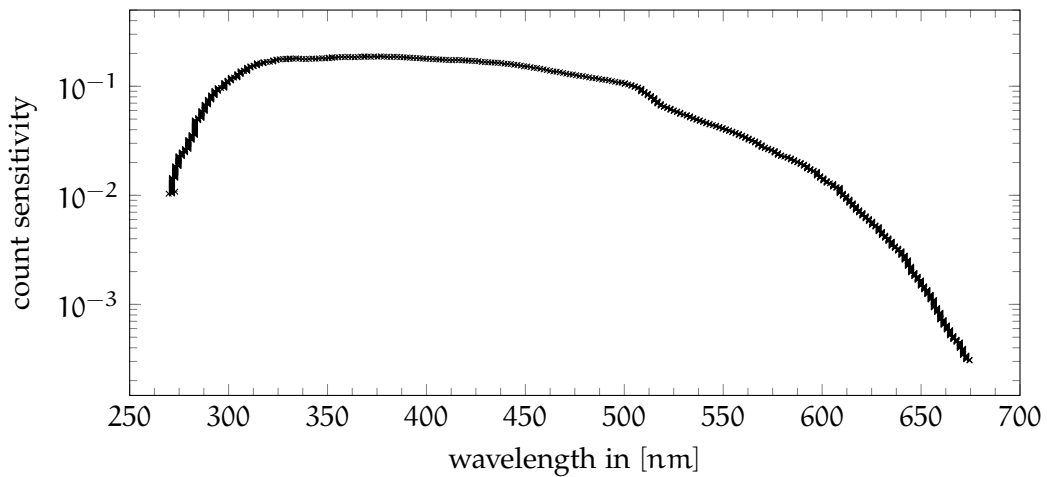


Figure 7: wavelength dependant count sensitivity of the μ PMT [16]

In figure 7 one can see the count sensitivity of the μ PMT for different wavelengths. The data is taken directly from the data sheet provided via Hamamatsu[16]. We can see that the efficiency is still at the peak of roughly for 450 nm our laser.

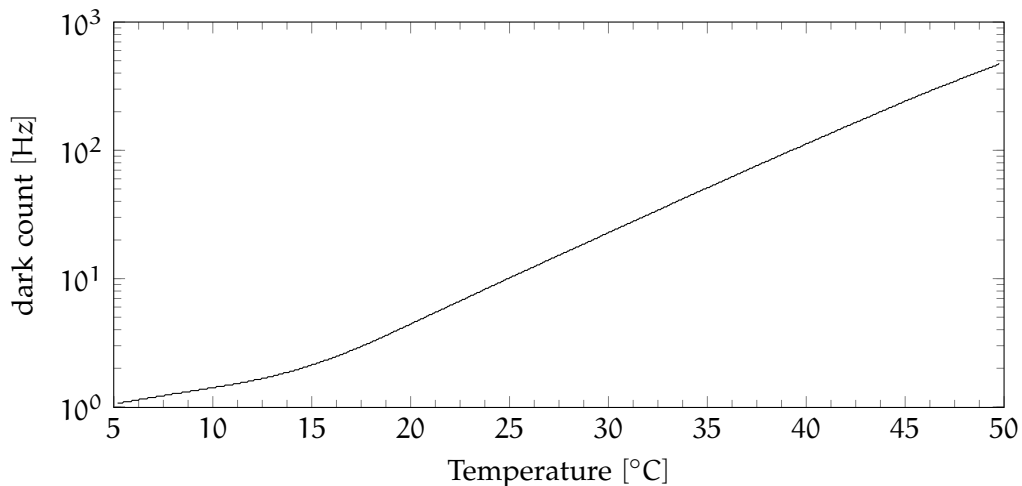


Figure 8: Dark count measured by Hamamatsu[16]

One advantage of PMTs is the extremely low dark count rate compared to e. g. SiPMs. In this case the dark count is between 1 and 50 Hz (See fig. 8) and since our μ PMT will operate at temperatures of a few $^{\circ}\text{C}$, we expect its dark rate to be at to lower limit of the provided values.

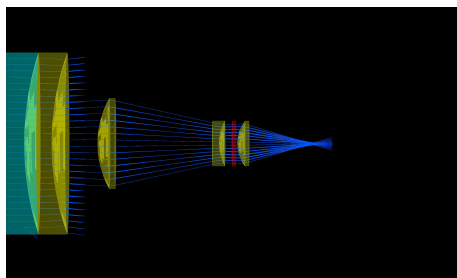
3.3 THE OPTICS

In this section I will describe the housing of the LIDAR and the optics. Its design was one of the primary goals of this thesis. It is based entirely on the results of the pyOpTools study described later in this thesis. The whole housing is made of AlMg₃ with a thickness of 2 mm. It is a standard alloy used for manufacturing and industry.

HOUSING V1

In the course of this thesis, I developed two designs. However, the general idea stayed the same. I wanted to keep it as simple and flexible as possible. I used an outer tube in which I stacked smaller tubes. They have a small cut-out at the end in order to hold the optical component. These tubes then got stacked inside the outer one, step by step filling the entire length (See figure 11b for reference). A ring closes the system, so the inner tubes were fixed in their position. This allowed us to build inner tubes with different lengths, so the position between the detector and the focusing length can vary. This is necessary for testing in the air because of the different focal length of the system in water compared to air.

In the first version I used a 2" Plano-convex lens ("LA1050-A") a focal length of 100 mm, than a Plano-concave lens ("LC1715-A") in order to defocus the rays that they hit the filter perpendicular and after that the filter and a last Plano-convex lens ("LA1422-A") to finally focus the beam onto the detector (See images 9a and 9b for detail and table 1 for information on the lenses). The names of the lenses are Thorlabs-specific product codes and apply only for their lenses.



(a) A side view of the housing v1 from the pyOpTools simulation



(b) Image of the assembled version of the housing v1 together with the laser.

Figure 9: Images of the first housing version.

NAME	DIAMETER	FOCAL LENGTH	BACK FOCAL LENGTH
LA1050-A	2"	100 mm	93.3 mm
LA1422-A	1"	40 mm	35.7 mm
LC1715-A	1"	-50 mm	-52.3 mm
LA1134-A	1"	60 mm	56.7 mm

Table 1: Information for the lenses provided by Thorlabs

While not exceeding the spatial limitations of the sphere. The major disadvantage of this optical design was the point spread function (PSF). Since I wanted to use a SiPM in the beginning, this would not have been a problem, because it was large enough to still cover the whole PSF. After building the housing, I realised that I would not be able to use the SiPM, mainly due to its high dark-rate and decided to use the μ PMT instead. Due to the small size of the μ PMT photocathode, I needed to redesign the optics in order to get a much smaller focusing spot.

HOUSING V2

In the second version, I needed to account for two new problems. The first one being the smaller effective area and the second one, the larger volume of the μ PMT compared to the SiPM. Therefore I went with the most simplistic design possible. At first the filter[22] and then a 1" Plano-convex lens with a focal length of 60 mm[23] (See also table 1. The filter has a central wavelength of 450 nm and a full width at half maximum of 10 nm. Figure 10 shows an exemplary plot of a premium bandpass filter compared to the normal ones sold by Thorlabs. The transmission is almost at 100% in the desired region and drops almost instantly to zero outside of it.

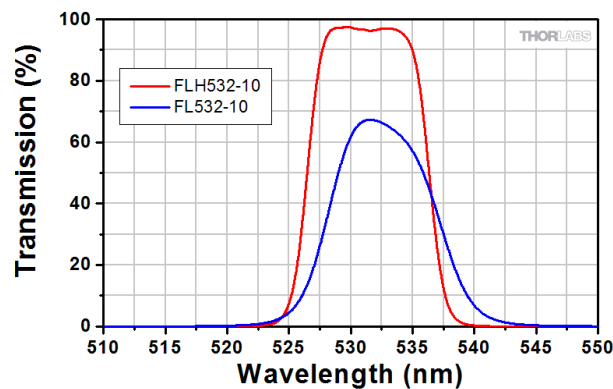


Figure 10: Comparison of a normal filter to the premium filter I use. Red is the premium filter.[22]

When one needs to focus light onto a single point, lens aberrations come into play. These can be divided into "monochromatic" and chromatic aberrations.

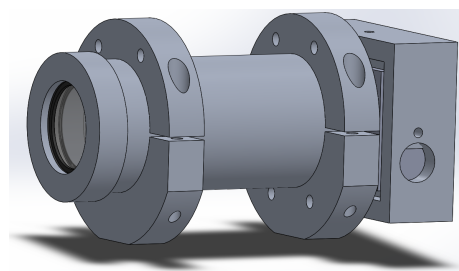
Since our μ PMT will only detect monochromatic light, I do not need to worry about the latter one. For monochromatic aberrations, the following are the most common one:

SPHERICAL It occurs with spherical lenses. Off-axis rays are focused closer to the lens than on-axis rays. Therefore the focus "point" is a line, not a point. Correction: Aspheric lenses; They are specifically designed to counteract this aberration.

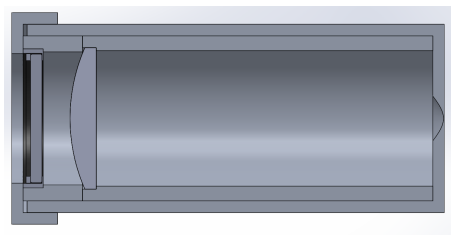
COMA It occurs when parallel light hits the lens non-perpendicular (called field angle). The rays will be focused on the same plane (given now spherical aberration) but with different heights from the optical axis. This produces the characteristic conical shape. Correction: using Plano-convex lenses

ASTIGMATISM Off-axis rays coming from different planes have different foci. Correction: Limiting the field angle of the system, using multiple lenses with opposite sign astigmatism

From those three aberrations, the only one relevant for us is the spherical aberration because the tilt of the laser beam is chosen in such a way that the laser beam is roughly at the optical axis compared to the distance between the scattering point and the LIDAR. Therefore the field angle will always be roughly zero. The simulation and its results will be described in chapter 4 in more detail. The drawback is that the field-of-view of this construction is reduced compared to the former one. However, even with a smaller field-of-view, the laser will most likely still enter it before I desaturate our detector. Image 11b shows the final design of the housing. As one can see, the concept stayed the same as for version 1: Inner tubes with a small cut-out for the optical components placed inside an outer tube which is closed with a ring. On the other side, I were able to reduce the length of the whole LIDAR (including the μ PMT) to less than 100 mm, which gives us more room inside the sphere.



(a) The final design for the LIDAR. Not shown: The frame for the laser



(b) The housing v2 as it was designed in Solidworks, lens and filter included, side view

Figure 11: Images of the final housing version

PMT HOUSING AND LASER MOUNTING

In the last part, I will describe the mountings for the μ PMT and the laser. The laser is mounted on a rectangular frame that (in the end) will have a slight tilt so that the laser beam will be sent in the simulated direction (see section 4.2.3 for details). This frame will be mounted to the housing via a clamp. This allows for free positioning of the laser along the tube.

The idea for the μ PMT housing was to make it as adjustable as possible in order to counteract errors during the assembly. Inside the housing four aluminium plates were placed on each side of the μ PMT (not on the front and the back since it was technically not possible). Each of those plates had two brass pins for stabilization and an M3 screw in the middle in order to move it forth and back. Each of these plates can be moved by 1 mm. In the following drawing, I can see the the housing for the μ PMT as it was build:

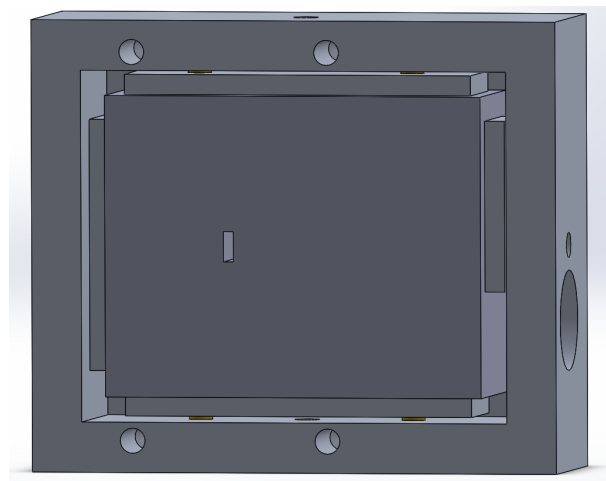
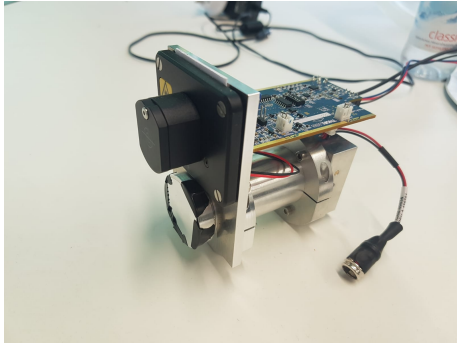
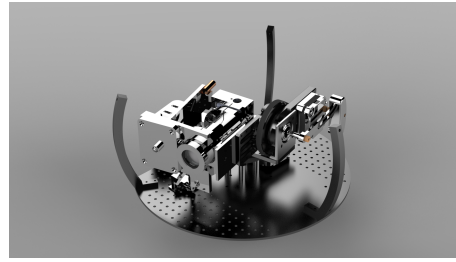


Figure 12: Front view one the housing of the μ PMT and inside a simplified version of the μ PMT

Moreover, in image 13a, one can see the final configuration of the LIDAR. Note that, the frame for the laser is not the final one but a temporary solution. The tilt of the laser is still not included and only realized through a sheet of paper at the top. The final one was still not finished at the time of the thesis. Secondly, I put a foil in front of the LIDAR. It only transmits 1 % of the light intensity and therefore protects the μ PMT from potential damage because of constantly too high light intensity.



(a) Final LIDAR with the configuration for the first test



(b) Final LIDAR including the module, solidworks rendering

Figure 13: Images of the final LIDAR

Part III

SIMULATION AND RESULTS

This part will focus on the Simulation and the first results of the LIDAR. 3 Different Simulations were written in the course of this Thesis. The first one using the `pyOpTools`-module for python, the second one using `geant4` were used to find the optimal configuration for the LIDAR. In contrast to them, the last ones focuses entirely on simulating the return signal that we expect given a optimal configuration of the LIDAR. This will be the first part. In the second part will be the first results shown.

SIMULATION

In order to know which optical design is the best for this setup and to generally learn more of what we can expect from our, several simulations were written. They will be described in the following sections.

4.1 SIMULATION OF THE LIDAR GEOMETRY USING PYOPTOOLS

4.1.1 THE PYOPTOOLS PACKAGE

The pyOpTools-package is a set of packages written for Python and Cython that allows simulations of an optical system via raytracing. It is written by the technological development group of Combustión Ingenieros S.A.S, and the applied optics group of the Universidad Nacional de Colombia.

The goal of this simulation was to find the most suitable optical configuration for the LIDAR. Since the effective area of the PMT is only 3×1 mm it was necessary to guarantee that backscattered light actually hits the detector. With this package, the user can build an optical system and can simulate the behaviour of light in this particular system via raytracing. But it has one major drawback: It can not simulate scattering events. So in order to simulate the path of the backscattered photons, a workaround needed to be created. The first idea was to reflect the laser beam after a certain distance with a "mirror", which has a curved surface to guarantee that the "returned signal" filled the lens of the optical system. A different approach was to set multiple detectors to varying distances from the origin of the beam and to see where the laser beam would go. After that, another beam would be sent back from the position of the initial one towards the optical system, so that one could see where it would be detected.

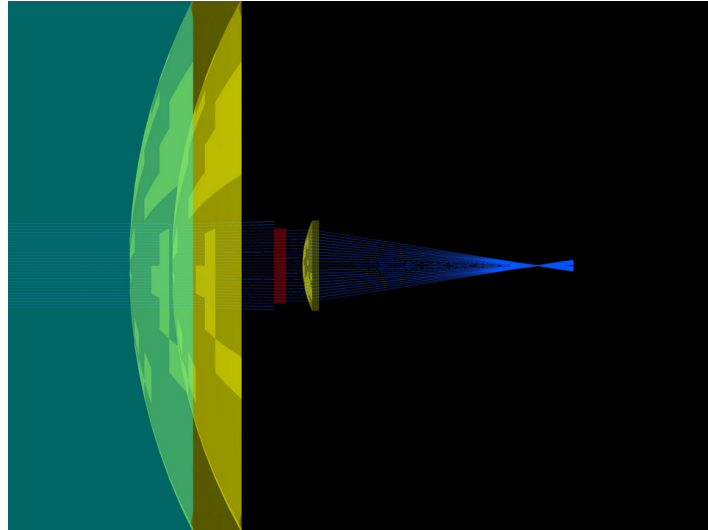


Figure 14: This picture was taken from the simulation. The cyan coloured lens represents the water, the big yellow one the glass sphere surrounding the module, the red one the filter and the small lens is the focusing lens. The returned light rays were made by the latter method described in the section

In figure 14 an image of the optical components is shown as they were designed with this simulation. The cyan coloured part on the left represents the water. It is composed of two "lenses". The first one is a cylinder-shaped block with the refraction index of water. It has a variable size, to simulate even hundreds of meters of water and next to it another "water lens" that fits tightly on the sphere. To simulate the round sphere, a meniscus lens is used. Whereby the inner and outer radius of curvature only differ in the thickness of the lens. The next component is the filter. It is a simple cylindrical block with the properties of optical glass (BK7 [29]). The last component of the optical system is the actual focusing lens. After many runs, a Plano-convex lens with a focal length of 60 mm (for details of the lens see [23]) with a distance of 64 mm to the detector gave the best results. For modelling the laser beam and also the returned beam, the "point_source_c" function of the pyOpTools package was used. Another thing worth mentioning is the coordinate system because it could lead to some confusion when comparing coordinates with the provided images. Here the z-axis is horizontally towards the right, the y-axis is vertically and downwards, and therefore the x-axis goes out of the drawing plane.

4.1.2 POSITION OF THE LIDAR PARTS

One of the primary goals of the simulation was to find the best distance of the lens and the filter with respect to the detector. The following values resulting from the study were used in Solidworks to design and build the LIDAR (See 3.3 for details). After various runs, 64 mm distance between the detector and the centre of the lens gave the best results. Whereby best results mean that the spot has the smallest diameter. As described in section 3.3, with the lens used for this LIDAR, a perfect focused spot will never be possible. In figure

15, a spot diagram, of what the detector would see, is shown. The expected diameter of the spot is roughly 0.30 mm. For this image, the point sources coordinates were $(0, 0, -149000)$, and its direction was along the z-axis. This, of course, does not represent the real situation because the optical system has a field-of-view and the laser beam will never be exactly on the optical axis. Therefore light not coming precisely from the optical axis of the system will still be detected. However, the purpose of this study was to find the optimal distance, so we assumed that the size of the spot will not change significantly for a beam, not on the optical axis. The opening angle was set to 0.009° in x- and y-direction and the beam consisted of 50×50 rays. This guaranteed that the whole filter got illuminated. A stopper blocked all rays that would not hit the filter (compare image 14; Although, due to its 2-dimensional shape, the stopper itself is not visible in the image). For comparison the same setup

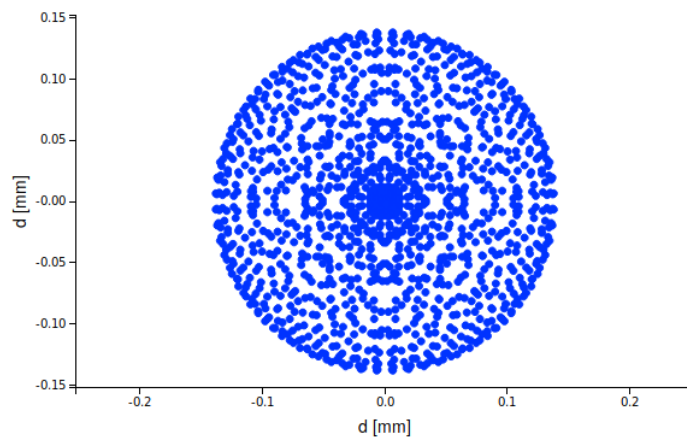


Figure 15: The detected spot size with 64 mm distance between detector and the centre of the lens

as in figure 15 but with a variation in the distance of ± 1 mm can be seen in figure 16. Clearly one can see that the diameter of the spot increases to about 0.4 – 0.6 mm. For a detector, that is only 1 mm wide, this is substantial increase. It could lead to rays not getting detected if other errors occur in the final system.

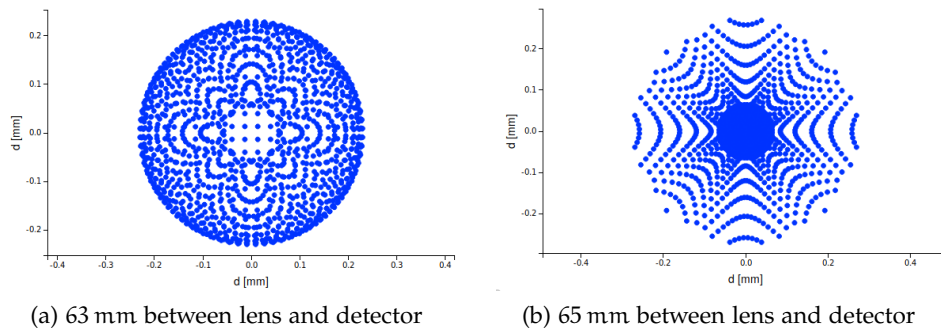


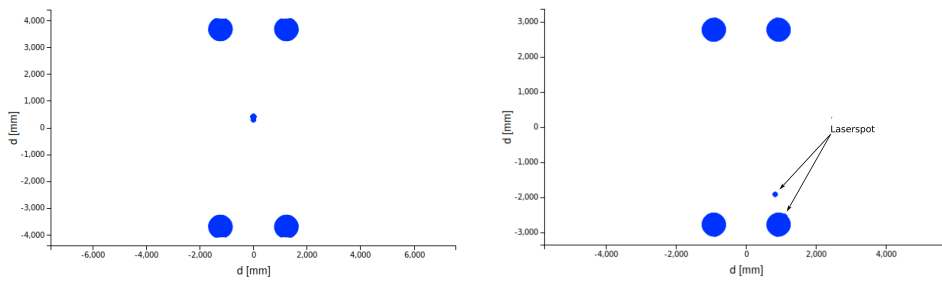
Figure 16: Same setup as in figure 15 but with ± 1 mm difference to the ideal position

4.1.3 IDEAL LASER POSITION

The second goal was to find the ideal tilt for the laser. To achieve this, the simulation was altered. The position of the laser source is parallel to the filter but with an offset of 44.5 mm from the optical axis. Its direction is still primarily the negative z-axis, but with a slight tilt "downwards" the positive y-axis. The opening angle of it, was set to 0.05° . This corresponds to at least a factor 5 more than what we would expect (see 5.1). Furthermore, four more sources were added, each of them at a corner of the detector, with an opening angle of approximately 25.2° . This angle assured that the whole lens got illuminated. The direction was again the negative z-axis. Those spots acted, therefore, as the boundaries of the field-of-view. Every beam within this area will reach the detector. To reduce unwanted refractions, a stopper was set up right after the "sphere".

Another thing worth mentioning is, that the spots in e.g. the images 17a or 17b are clearly not completely round shaped. The most likely explanation for this is that not all the light get transmitted but a few percent gets reflected instead. If this happens twice in the same object and the angle of incident is not exactly 90° , the reflected light would still propagate in the same direction as the rest of the rays but with a slightly different angle. A consequence of this is that the laser light will sometimes have two spots in the plot. But due to the limited resolution of the images the main beam can not be identified.

With that said in the following two images, the results are plotted. In image 17a with the ideal tilt of the source and in image 17b with the maximum offset that the PMT would still detect the backscattered light. It yielded a tilt of $6(1)^\circ$ in the y-direction and a tilt of $0.0(4)^\circ$ in the x-direction.



(a) The Laser beam is in the ideal position. (b) The Laser beam is in the last possible position ($+1^\circ$ vertically and $+0.4^\circ$ horizontally) in which it is still in the field-of-view

Figure 17: Image of what a detector at 149 m distance to the LIDAR would see. The big spots are marking the corner of the field-of-view of the detector and the small one the laser beam.

The centre and the length of one side of the Spots are roughly:

Ideal laser tilt:	$(0, -735), 130 \text{ mm}$
Maximum laser tilt:	$(1082, -3382), 130 \text{ mm}$

Something important to note: The "laser beam" spot that is visible in 17b is actually not the primary beam spot. It is the second spot caused by the reflection on the sphere. The primary spot is not visible because it is already at the boundary of the spot in the lower right.

To show what the detector would see, the following image shows a plot of a returned beam from a point that lies within the laser spot of figure 17b. As one can see, most of the signal would still be inside the area of the PMT, but the corner of the spot already passed the 0.5 mm which marks the edge of the detector. Unfortunately pyOpTools does not provide a possibility to analyse the detected photons, so no accurate percentage of how many photons would be missed, could be provided.

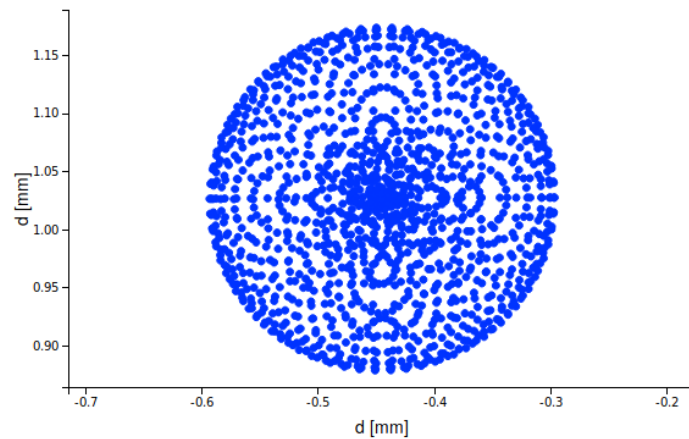


Figure 18: The detected spot size with 64 mm distance between detector and the centre of the lens and a maximum offset for the laser described before

4.1.4 MAXIMAL POSSIBLE OFFSET

In this section we will take a look at the results when the lidar is not perfectly aligned with the optical axis. In addition also the behavior of the laser will be shown, when it has a deviation from the ideal position.

In the following figures the offset only along the z-axis is shown. x- and y-direction stays aligned with the optical axis. For comparison: In all the other figures a standard offset of 50 mm from the centre of the sphere was assumed. This will most likely be close to the final offset.

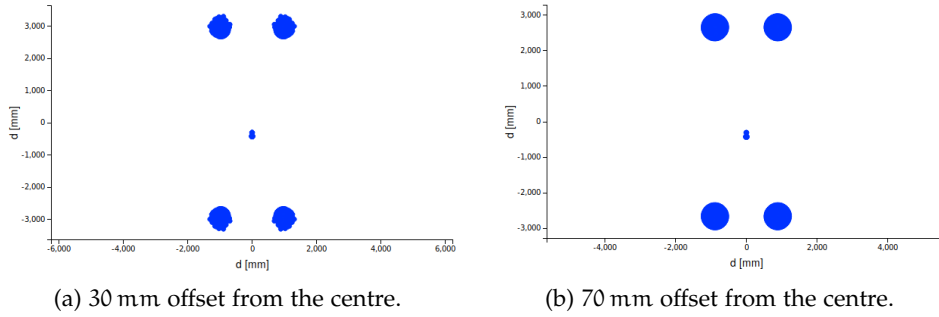


Figure 19: The laser is in the ideal position described above and with a varying offset of ± 20 mm difference.

As one can see the laser spot is very stable, although the covered distance of 40 mm is a lot larger than the expected uncertainties, we will be facing when the final lidar will be assembled. If one accounts for the maximum uncertainties of the laser, the following images are to be expected. Note that these offsets needed to be adjusted as followed to guarantee that the spot is still in the area of the detector. For the 30 mm the error in the y-direction needed to be reduced to 0.5° and for the 70 mm the maximum error in the x-direction the error was set to 0.3° . All the other errors were not changed.

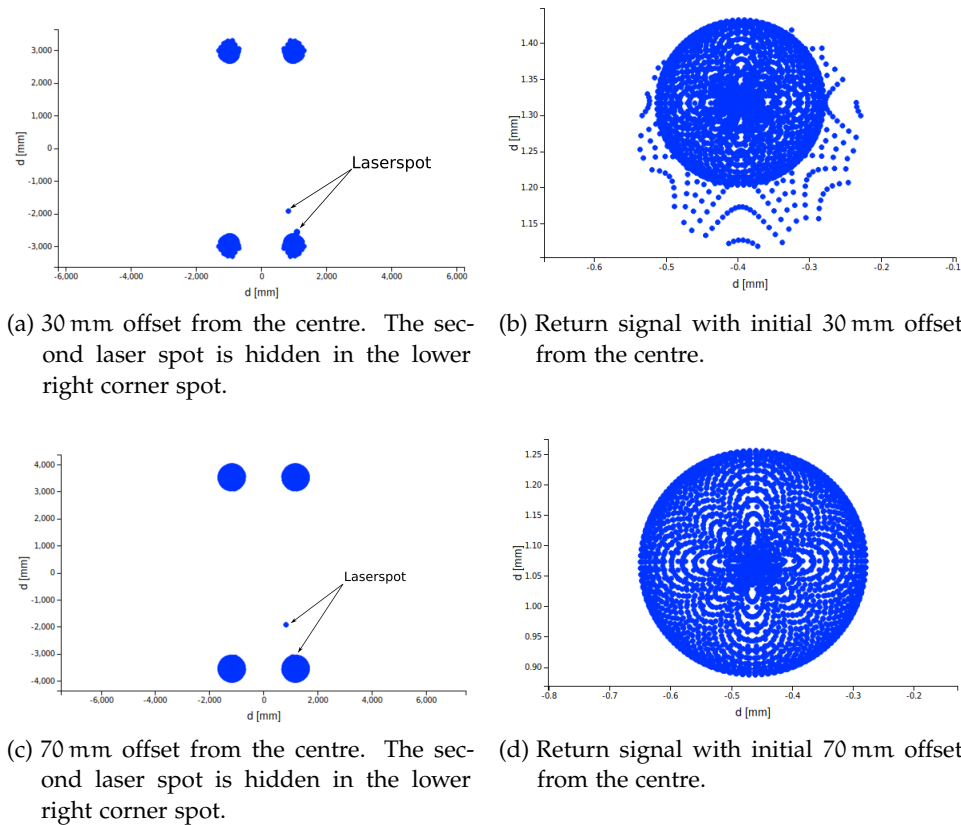


Figure 20: The laser beam with the offset described above and with a varying distance along the z-axis of ± 20 mm from the ideal position.

In image 20b a kind of corona is visible that would partially not be detected by the PMT. But given that it only consists of a few hits, the majority of the light should still be detected. So, as long as the LIDAR does not move to far away from the ideal position of 50 mm distance to the centre of the sphere and along the z-axis, the limits for the errors of the laser tilt stays correct.

We have now looked at the offset in z-direction and did not change it in x- and y-direction. In the following this will be reversed and the offset along the z-axis will be kept at the initial value of 50 mm. In the Images 21a - 21b are results for 10 mm and 20 mm offset shown. With a offset of 10 mm almost no relative deviation to the image 17a, were everything is in the ideal position, can be seen.

But when compared to the 20 mm offset it has unnelectable shift both for the spot at 149 m and of the returned signal. Therefore from this simulation a maximum deviation of around 10 mm should not be exceeded.

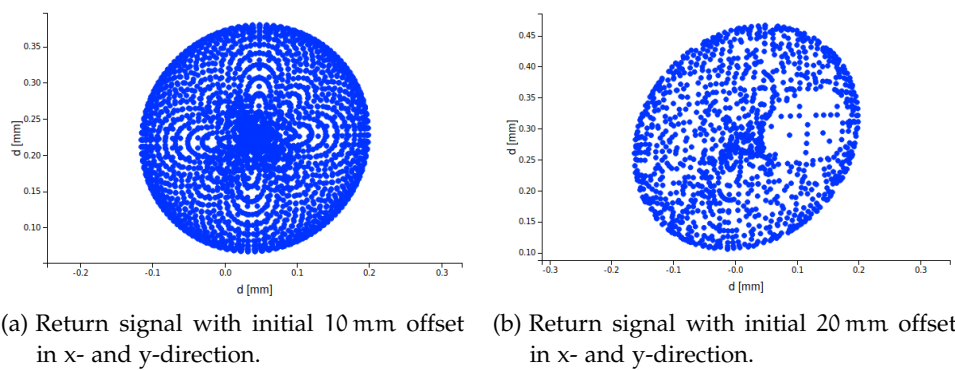


Figure 21: The laser beam with the offset described above and with a varying offsets in the x- and y-direction

Another significant difference to point out is the absolute difference to the ideal plot. In the ideal plot, everything was (obviously) centred around the origin with a field-of-view of roughly 3 m along the y-direction and 1.7 m on the x-direction. For both offsets the dimensions of the field-of-view stayed roughly the same, but it got shifted by 3 m along the negative x- and y-axis for 10 mm offset and as much as approximately 7 m for the 20 mm. Note that those values are just estimates based on the images and exemplary. Depending on the direction of the offset, those values will change their sign.

For the core mechanics of the LIDAR, this phenomenon plays a minor role, because primarily the LIDAR will shoot in any direction of the hemisphere. However, one different application for the LIDAR could be to shoot in the direction of the other modules to get their exact position. In order for this to work, the general offset of the field-of-view should not exceed a few centimetres in a distance of tens of meters. If we assume that the offset should not be greater than 100 mm after a distance of 50 m and everything scales linearly than the maximum possible offset needs to be less than 1 mm which will be most likely not achievable. Additionally the mechanics of the modules and the

strings and their tilt in the water will not be precisely known. Again this needs to be estimated by hand, because of the data structure of this function. The centre of the spot in the ideal position is at $(0, 218)$ (all at a distance of 50 m and in units of mm)). But with a deviation of 1 mm in both directions the centre of the spot moves to $(-118, 86)$. This is already beyond the required limit of 100 mm maximum in any direction.

4.1.5 VERIFICATION ONLY IN AIR

In the last section for the pyOpTools simulation, we will go more into detail about the accuracy of this simulation. To do this, we took the simplest possible example. We sent a (approximately) parallel beam onto the lens without any water, sphere or filter and looked after which distance the beam was most focused. According to Thorlabs for the lens we used, the back focal length is set to be 56.7 mm[23]. Those measurements are relative to the rear surface of the lens. So in our case from the flat side. Since in pyOpTools all measurements are done from the center of the object we expect the focal point to be at precisely at 59.05 mm ($56.7 \text{ mm} + \frac{4.7}{2} \text{ mm}$). But as we can see in figure 22 this is not the case for pyOpTools. The simulated focal length for the lens is a lot shorter than it was expected to be. After optimizing the best distance for this simulation was 56.5 mm from the back of the lens. This is a difference of 2.55 mm. In a lens Tutorial of Thorlabs, they claim that the spherical aberration causes the focal "point" to be as broad as almost 2.2 mm (in the z-direction) and as thick as $240 \mu\text{m}$ (in the x-y plane)[26]. Our observations are only consistent with the broadness of the focal point. The thickness of your spot exceeds the values provided by Thorlabs.

And the drawbacks of this simulation is again that the plot of the spots only shows the positions of the rays on the detector. However, due to the large spatial extensions of those spots, almost no information about the density of them can be retrieved. Therefore, the only information we get is the diameter of the spot.

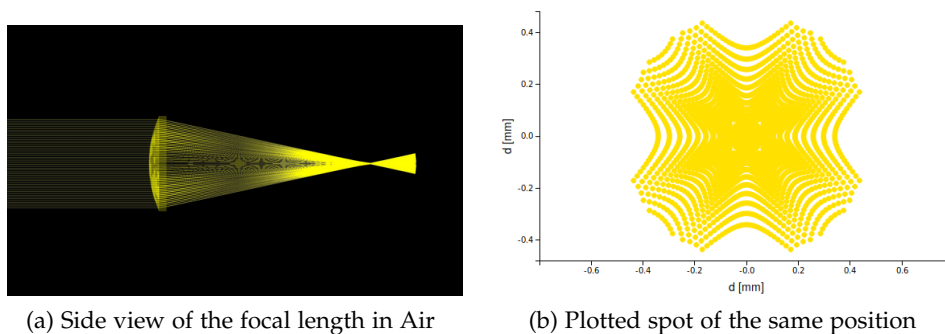


Figure 22: Side view and the detected spot for a distance of 59.05 mm from the middle of the lens.

These uncertainties and the lack of some information led to the decision to do a second simulation with the same goals with `geant4`. This simulation, alongside the results, will be the content of the next section.

4.2 SIMULATION OF THE LIDAR GEOMETRY USING GEANT4

In order to cross-check the results of the `pyOpTools-Simulation`, a second one was written using `geant4`. `geant4` is a Monte Carlo Simulation written and developed at the Cern. Its primary purpose is to accurately simulate the interaction between particles and matter. It is used in various high energy experiments like ATLAS, CMS or LHCb. However, it has also a vast variety of applications in other fields, e. g. in medical radiotherapy or for NASA and ESA space missions. Since it is also able to simulate optical photons and their behaviour, we decided to use it for a second simulation of the optics of the LIDAR.

A member of our group, Kilian Holzapfel, already wrote a simulation for a similar purpose, so with his permission, we decided to adapt it for the LIDAR. The general structure of this section stays the same as in Section 4.1 although there will always be a comparison between the results.

4.2.1 SETUP

Figure 23 shows an image of how the LIDAR was modeled in the `geant4` simulation. The first picture is directly taken from a 90° angle in order to better show the positions along the z-axis and in 23b the same setup but with a more titled view than in 23a so the position and size of the detector (cyan) can also be seen.

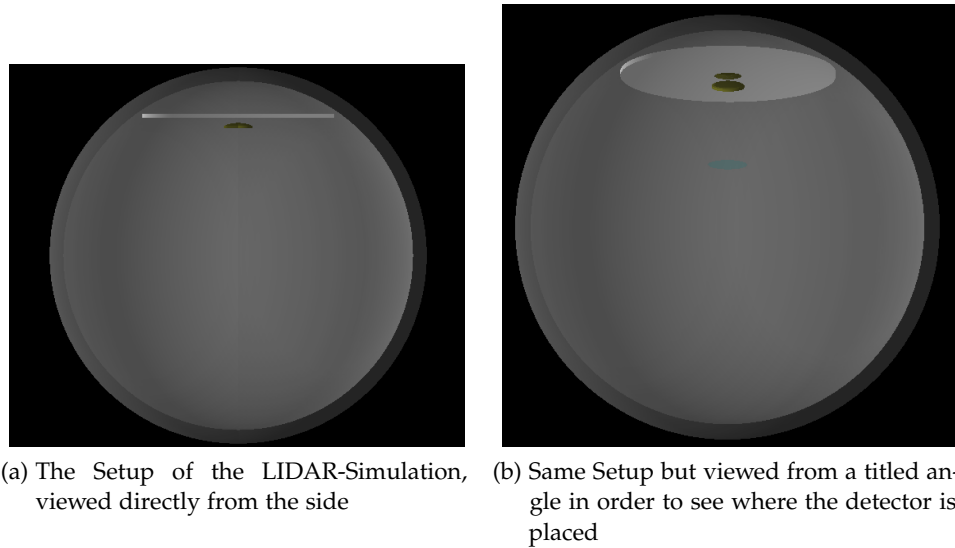


Figure 23: Two Images of the LIDAR-Setup in the Geant4 Simulation. Black Area represents the Water, the darker grey the Sphere and the lighter grey area inside the Air, in Yellow the lens and the filter, in Cyan the detector and the white area around the filter a (not existing in the real module) ring in order to absorb any rays that would miss the detector.

So the simulation is build up as followed:

- An outer sphere is setting up the world. It is filled with water which has a refractive index of 1.3375 (at 450 nm)
- A Sphere with an outer radius of 165.1 mm and an inner radius of 153.1 mm made of Pyrex with a refractive index of 1.480. In the image 23 represented by the dark grey shaded area
- The inside of the Sphere is filled with air which has a refractive index of exactly 1.00 (The lighter grey orb)
- For the LIDAR itself, only the focusing lens and the filter alongside the detector were left. The first two parts are the yellow objects in image 23 and the detector, a (approximately) circle, in cyan and due to the 2D shape only visible in 23b.
- The last component, the white cylinder with the same thickness and at the same position as the filter, acts as an absorber. It is made of a fictitious material with an absorption length of 0.00 mm.

The positions and the sizes of the LIDAR parts are the same as described in section 3.3. The material of both the lens and the filter is "N-BK7". The real lens is made precisely out of this material, but Thorlabs does not provide any information for the filter. However, given that the backscattered light is far away, the angle of incidence of the light rays on the filter is small, and the light will hit the filter approximately perpendicular, refraction will not play a significant role and therefore a different refractive Index will not change

the accuracy of the simulation. Furthermore, for this simulation, the chemical composition of the materials does not matter because only refraction and absorption are used. However, we decided to model the materials still as accurately as possible. So we took the composition for BK7 from [1] and for the refractive index we used the coefficients B_1 , B_2 , B_3 , C_1 , C_2 and C_3 from the official datasheet from Schott for N-BK7[29] to calculate the refractive index via the "Sellmeier-Equation"[21].

$$n(\lambda)^2 = 1 + \frac{B_1\lambda^2}{\lambda^2 - C_1} + \frac{B_2\lambda^2}{\lambda^2 - C_2} + \frac{B_3\lambda^2}{\lambda^2 - C_3} \quad (4.2.1)$$

This equation is an empirical representation of the wavelength-dependent refractive index for a transparent material.

In contrast to all the other components, the absorber is the only one that was implemented for the sole purpose of simplification. It mimics the real situation, where all the light rays that do not hit the filter will not reach the detector either. Two other reasons why we went with this geometry were that it, on the one hand, also prevents the situation that light rays which are backscattered at the bottom of the sphere would get detected too, and on the other side, compared to e. g. modelling the complete housing of the LIDAR, it is the simplest solution implementation-wise.

The last significant difference between the simulation and the actual system is the size of the detector. As described in section 3.2 the detector only has an effective area of 1×3 mm. But in order to still see the point where the light rays would have hit the detector, we decided to use a round-shaped geometry with a radius of 15 mm for the detector.

As already mentioned at the beginning of this section, the main reason for this simulation was to cross-check the pyOpTools simulation. geant4 has the advantage that it can also simulate Rayleigh- and Mie-Scattering, so the second idea was to use this and combine the pyOpTools and the return signal simulation and put it into one single simulation. However, unfortunately, due to the limited time, it was not possible to implement this combination. So we went with the same approach as in the pyOpTools simulation and split the simulation into two steps. In the first step, a source, that is roughly placed at the position where the real laser will be, shoots light rays into the water. Those light rays get detected with a second detector, which is shaped like the one mentioned above, just with a bigger radius. In the next step, the position, the centre and the diameter of this spot then get saved into a file. Everything after saving the detected hits is then done externally with Python. In the last step, the saved parameters act as an input for a second source with a circular shape. This shape is configured in such a way that it always points towards the centre of the sphere, i. e. (0,0,0) since the whole simulation is spherically symmetric around the centre, and the opening angle is so big that from any point on the surface of the circle the whole filter gets illuminated. As long as not stated otherwise 10 Million Photons were used for every run.

4.2.2 POSITION OF THE LIDAR PARTS

In this section the position of the filter and the lens in respect to the detector will be shown. The pyOpTools Simulation led to the following positions (all to the centre of the object):

LENS (0,0,64 mm)

FILTER (0,0,72.65 mm)

For verification, the same conditions were used as in section 4.1.2. A point source on the optical axis and 149 m away from the origin. These are the results for the ideal position, followed by two plots for a deviation of ± 1 mm:

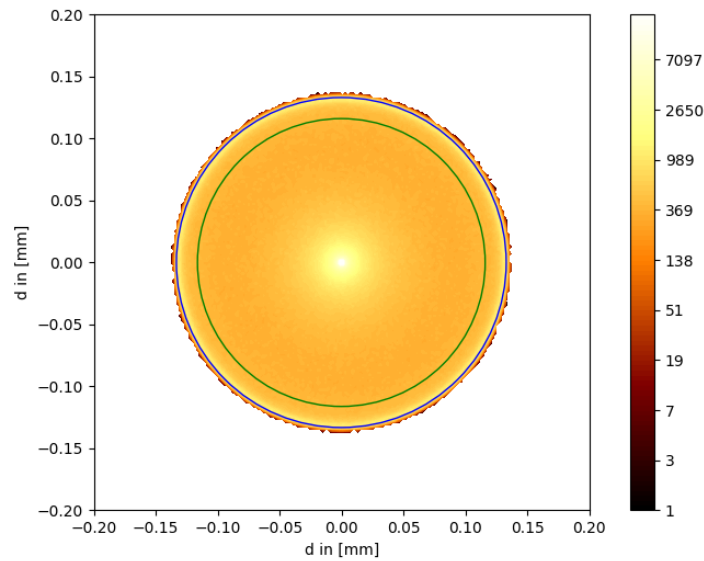
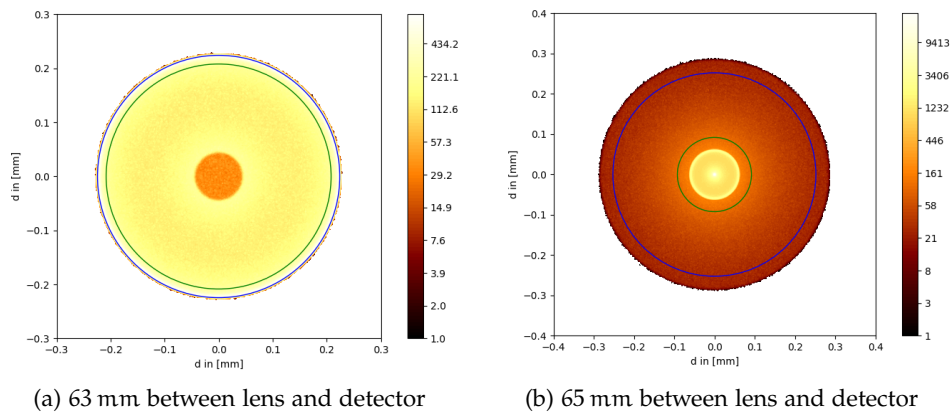


Figure 24: The detected spot size with 64 mm distance between detector and the centre of the lens. The green circle marks the area where 68.3% of the detected photons are included and the blue circle the area with 95.5%. This will be the case for all following figures.



(a) 63 mm between lens and detector

(b) 65 mm between lens and detector

Figure 25: Same setup as in figure 24 but with ± 1 mm difference to the ideal position

From the images, the detected signal is identical to the one shown in 4.1.2. A explanation for the small differences, especially in 16b compared to 25b, could be that the initial difference in the laser beams. For the pyOpTools simulation the beam is always a square with a specified number of photons along each axis, e. g. 50 in this case, but in geant4 the rays get equally distributed in a circular shape. However, in contrast to the former simulation were the information of the detected signal was written in a special format and properties of the spot needed to be guessed from the image, the analysis for this one uses numpy ndarrays entirely. This is an easy to handle datatype and gives the option to retrieve further information, e. g. the exact position with the highest counts or the diameter of a circle around it that a certain percentage, e. g. 90 %, of the detected photons are included. For the images 24, 25a and 25b this yields the following values:

Distance detector - lens	centre	diameter
64 mm	(0,0)	0.26 mm
63 mm	(0,0)	0.38 mm
65 mm	(0,0)	0.36 mm

Table 2: For the three simulated distances their centre and the diameter of a circle, which contains 90 % of the detected photons

The values of the table are the same as the guessed values of the pyOpTools simulation. The only difference is the value for 25b which is lower. This is also the image which does not match the counterpart in 4.1.2. A second explanation could simply be the higher statistics. For pyOpTools only 50×50 Photons were used compared to 10 Millions in geant4.

4.2.3 IDEAL LASERPOSITION

In Section 4.1.4 the ideal tilt for the laser was found to be $6(1)^\circ$ in y-direction and $0.0(4)^\circ$ in x-direction under the condition that the offset of the whole LIDAR stays less than the examples in 4.1.4.

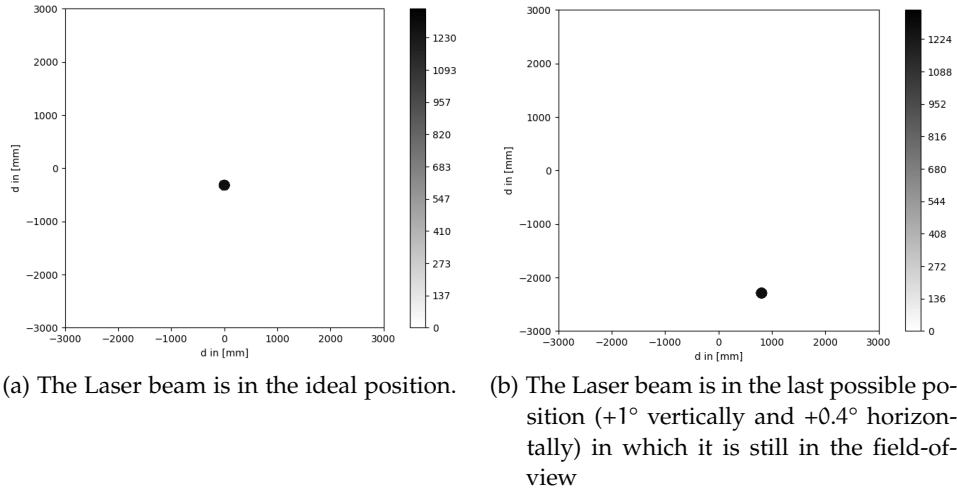


Figure 26: An Image of what a detector at 149 m distance to the LIDAR would see.

It yields the following positions of the centre and the diameter of the circle:

Ideal laser tilt:	(0, -320), 192.2 mm
Maximum laser tilt:	(806, -2291), 192.2 mm

Compared to the values simulated with pyOpTools, a notable difference both in the position of the centre and the size is present. The values from geant4 are by 25% - 56% closer to the origin. For the ideal laser position, this can easily be ignored because the spot is still somewhat close to the centre. But as one can see when comparing image 18 with 27a the spot moved even further away from the centre. This is especially noticeable along the y-axis. The pyOpTools simulation gives a centre value of approximately 1.15 mm whereas geant4 yields 1.24 mm. Nevertheless, the spot is still mostly inside the range of the detector. So the conclusion from the pyOpTools simulation for the maximum deviations of ±1° in y-direction and ±0.4° in x-direction is confirmed. Although due to the vast amount of other uncertainties this limit should not be reached to guarantee that the spot stays in the reach of the detector.

Another interesting phenomenon worth mentioning is the few detected photons in image 18 that were seemingly randomly outside of the expected circle got confirmed with this simulation. The same deviation happens in the geant4 simulation, but due to the higher statistics, it is visible that those few photons were not just random errors in the propagation code of the simulation.

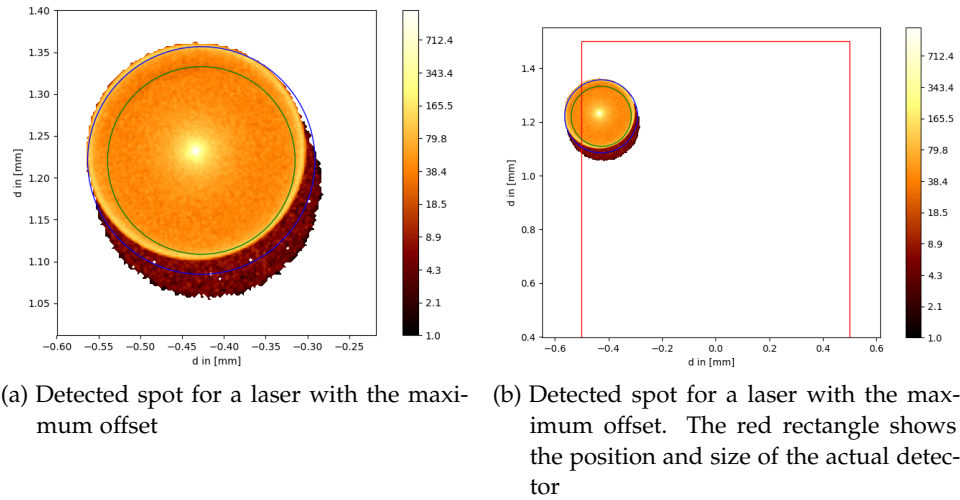


Figure 27: A detailed and a view with the detector for comparison of the detected spot size with 64 mm distance between detector and the centre of the lens and a maximum offset for the laser described before.

4.2.4 MAXIMAL POSSIBLE OFFSET

This section will follow the same structure as 4.1.4. At first we will look at the impact of a different position of the lidar along the z-axis and after that along the x- and y- direction and look how it changes the position of the detected laser beam spot.

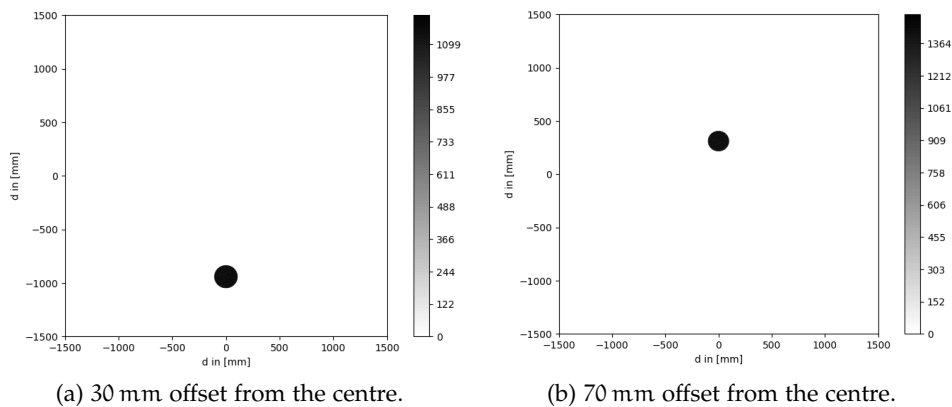


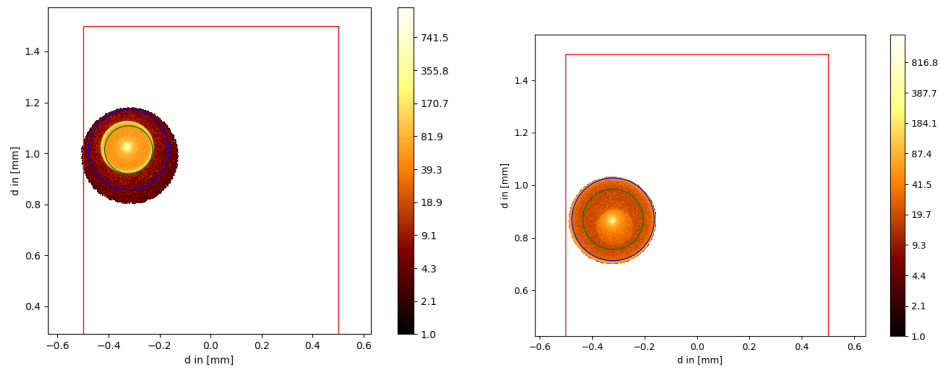
Figure 28: The laser is in the ideal position and with a varying offset of ± 20 mm difference.

The spots are now located at $(0, -941)$ for the 30 mm and $(0, 310)$ for the 70 mm. pyOpTools yielded the following values for 30 mm and 70 mm respectively: $(0, -1550)$ and $(0, 95)$.

It follows a similar trend as in the section before. However the values from geant4 are now constantly too high and on the other side the difference be-

tween these values are now smaller.

If we plot the detected photons too, we get the following images:

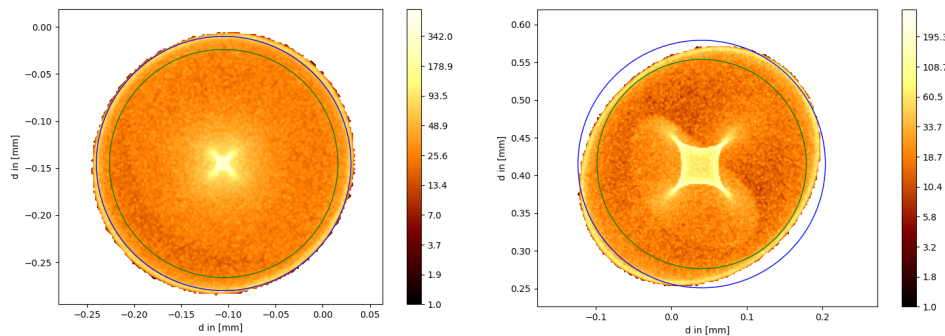


(a) Return signal with initial 30 mm offset from the centre. (b) Return signal with initial 70 mm offset from the centre.

Figure 29: The laser beam with the offset described above and with a varying distance along the z-axis of ± 20 mm from the ideal position. The red box marks the edge of the detector.

The laser error for the 30 mm needs to be reduced by 0.5° in y-direction and by 0.1° in x-direction to ensure that the returned signal is still in the reach of the detector and for the 70 mm we needed to reduce the x-direction error to 0.3° . These adjustments are the same as in the pyOpTools simulation. Again the pattern stays the same. The spots are roughly on the same positions but not quite. For the images of 29 the values of the laser beam are all closer to zero.

In the second part of this section, we reset position on the z-axis to 50 mm and just look for the uncertainties in the x- and y-direction. We then get the following images:



(a) Return signal with initial 10 mm offset in x- and y-direction. (b) Return signal with initial 20 mm offset in x- and y-direction.

Figure 30: The laser beam with the offset described above and with a varying offsets in the x- and y-direction

Those images again confirm the predictions of pyOpTools. Especially the elongation in the images 21b and 30b are very similar to each other. But as

already mentioned in the other sections the positions of the spots are not the same although they still follow a general trend. Again the values of the centre of the spot are closer to zero for geant4 than for pyOpTools.

4.2.5 VERIFICATION ONLY IN AIR

As we have seen in section 4.1.5, the pyOpTools simulation gave a surprising result as it did not match the data provided by Thorlabs at all. For the geant4 simulation, we tried the same setup. Only the lens, an approximately, parallel ray beam and the surrounding made out of air. The maximum focused spot was detected after 57.5 mm. This is an interesting result because Thorlabs claims that this value is the back focal length. However, they always measure focal lengths from the end of their lenses[27]. So according to this, 59.05 mm should be the distances with the smallest spot. But the simulation yields the following values:

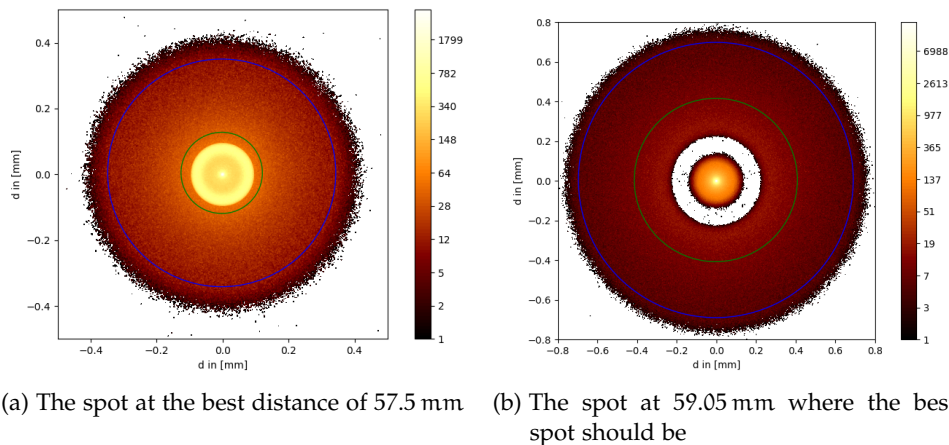


Figure 31: Side by side comparison of the best spot and where the best spot should be.

An important note: As already mentioned in section 4.1.5, the provided values of Thorlabs are always measured with the Helium D-line (587.6 nm). In order to reproduce those values, the wavelength of the laser beam was changed to this value.

When comparing the images of 31, we can see the effect of lens aberration. 31b is at the distance of the provided focal point. We can see a focused point in the middle, but it is surrounded in a corona. This is due to spherical aberration. Off-axis rays get refracted stronger than on-axis rays. Therefore they cross the optical axis earlier. However, this effect is minimised at roughly 57.5 mm (which means 1.55 mm less than the back focal point). An image of the focused spot can be seen in figure 31a.

4.3 COMPARISON OF THE SIMULATIONS

After we compared the results of the two simulations, one phenomenon was always present. The positions of the spots, both of the laser and the returned signal, are always different, and the values of the geant4 simulation are almost always closer to zero than those of pyOpTools. For this, we came up with two possible explanations. The first one is a slight difference in the optical properties of the components. But this can be excluded for the lens and the filter. The refractive index is in both cases provided via the Sellmeier equation with the same coefficients. However, the water and the sphere are not that precisely defined. Small deviations in the indices could lead to slight different refractions that would be only noticeable after long distances, and in both simulations, we deal with vast distances between the starting and the detection point of the laser beam. The more extreme values from pyOpTools could, for example, be explained with a slightly higher refractive index of the sphere compared to the one in geant4. But on the other side this would mean that the images 22b and 31b should yield the same results because, in both simulations, only the lens plays a role. Especially for the diameter of the spot, since the focus cannot be checked in pyOpTools. geant4 gives a precise diameter of 1.36 mm, whereas the diameter of the pyOpTools simulation is roughly 1.4 mm. Those values are identical given the uncertainties from the pyOpTools simulation. Therefore we conclude that the differences most likely come from slightly different refraction indices.

4.4 SIMULATION OF THE RETURN SIGNAL

The goal of the pyOpTools and geant4 simulation was to find a suitable geometry for the LIDAR and to learn more about the behaviour of the optics. In order to do this, we had a high photon statistic, especially in the geant4 simulation, where we used up to 100 Million Photons per run. Therefore we completely neglected the underlying physics of the LIDAR. The goal of this simulation is to model as accurately as possible the number of photons and their time-profile we expect in each run. To do this, we now ignore all the optical parts and assume that every photon that should, in theory, hit the detector, actually hits it. The whole code of this simulation can be found in the appendix (section A).

In the first step, we estimated the background. For this, we needed the wavelength-dependent distribution function of the light at Cascadia Basin. However, at this point, we did not know this distribution, and in fact, it was one of the goals of STRAWb. Therefore we assumed a Gaussian distribution with the mean at 450 nm and a standard deviation of $\sigma = 150$ nm. This, of course, is a very simplified assumption. After multiplying this function with the count sensitivity of the PMT^[17] and cutting out everything that is not in the interval of 445 nm - 455 nm, we were left with an approximate dark rate of 1.59 Hz. This value was calculated by scaling the measured noise in STRAW

down to the LIDAR. Since we do not know the light distribution at Cascadia basin we assumed a gaussian with a peak at 450 nm and a deviation of 150 nm and folded it with the detector efficiency and only considered values in the interval 450(5) nm. To get the final noise, we multiplied the ratio of the value in the interval to the whole noise with the down scaled noise and added the dark rate specified from Thorlabs. (For details see the Python code in section A).

In the next step, we calculated how many Photons we would expect for each distance according to the LIDAR equation (2.2.1). For the attenuation coefficient α we choose the latest results of our STRAW measurements which yielded a attenuation length of $l_{\text{att}} = 26(3)$ m and therefore $\alpha = 1/l_{\text{att}}$. It was more difficult to choose an appropriate value the scattering coefficient β_{π} . Since we neither know the chemical composition of the water at Cascadia basin nor did we found any measurements in particular at a wavelength of 450 nm. We made the simple assumption that the LC scattering is roughly ten times larger than the SC scattering. We therefore assumed a value of $\beta_{\pi} = 0.011 \text{ m}^{-1} \text{ sr}^{-1}$.

For the final results, we sampled data points according to the PDF calculated from the evaluation of the LIDAR equation. Only photons with a minimum difference of 20 ns were counted. This is due to the pulse width and the dark time of 10 ns respectively. After that, the calculated background got added. Furthermore, for the measurements, we assumed a 500 khz trigger signal. The initial amount of photons was set to 1×10^9 . This corresponds to a pulse width of 14 nm according to the laser manual[24]. Another thing noteworthy is that the geometric factor $G(r)$ of the LIDAR equation is simplified to be 0 if the distance is smaller than r_{start} and 1 if it is larger. We calculated a value of $r_{\text{start}} = 2.36$ m. Since we saturate anyway for these close regions, this approximation is sufficient.

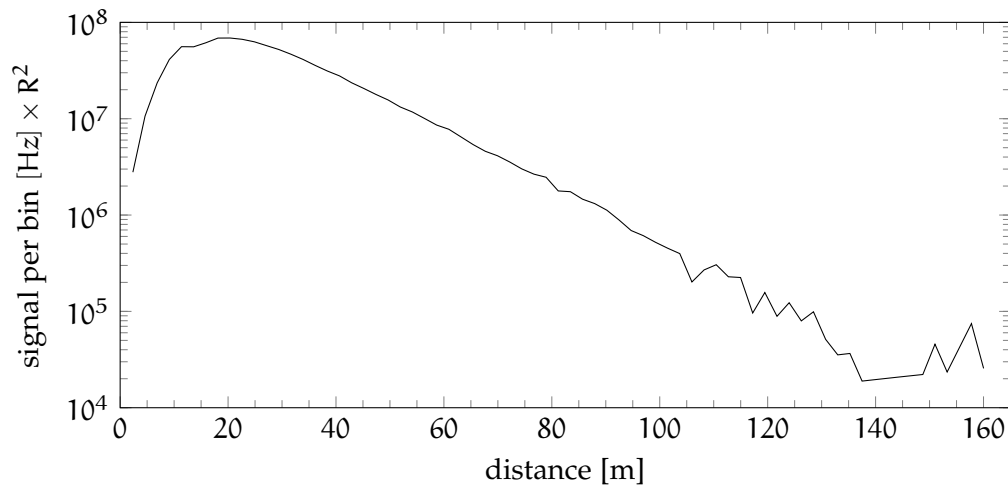


Figure 32: Range corrected return signal for 1 s of observation with the described settings.

From this plot, we can see that an evaluation of the signal is possible for distances from 25 m up to 100 m. Through the range correction, the slope of

the, in the logarithmic representation, signal is the attenuation coefficient α . However, this is only the expected rate for 1 s of observation. If we observe e. g. 60 s we get the plot in 33. Note that in this plot the cumulative rate is shown and not the average. Therefore also the unit changes from Hz to 1/min. Now the linear part extends up to 140 m. After that signal flattens out again and is dominated by background noise.

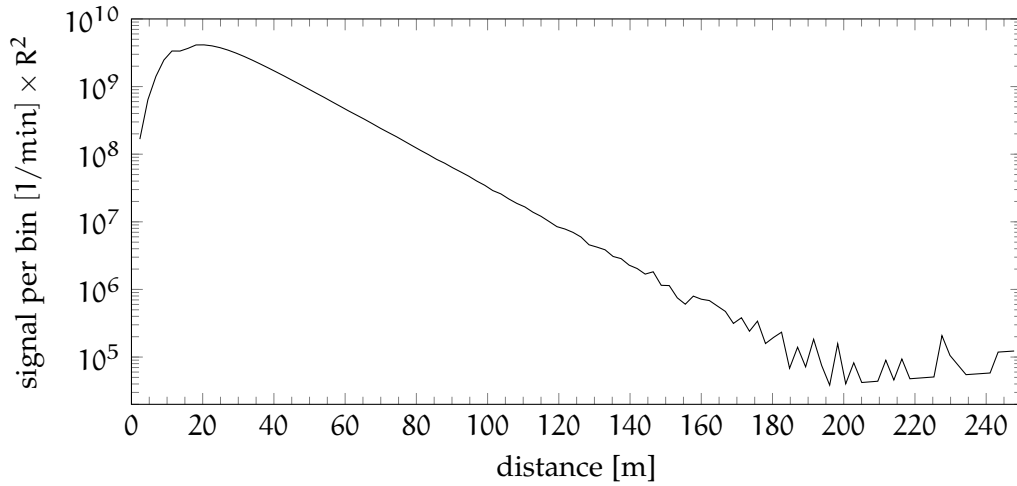


Figure 33: Range corrected return signal for 60 s of observation with the described settings.

RESULTS

In this chapter, we will present some of the first measurements that we performed with the LIDAR system. Due to time limitations in the scope of a Bachelor thesis and the and problems with the availability of some of the hardware components of the readout system, we could not do any more in-depth characterisation measurements like e.g. shooting into the sky and collecting a profile or assemble the system, put it in the sphere and take already first measurements underwater. This is expected to be done after this thesis and before the deployment of STRAW-b.

5.1 OPENING ANGLE OF THE LASER

The first measurement we did was to characterize the opening angle of the laser beam. Thorlabs provides no information on that, except for a beam point accuracy that is $\leq 3^\circ$ [24]. This is said to be the deviation of the beam axis normal to the plane of the front surface and only provides us with a general offset. However, it gives no information about the opening angle of the laser beam itself.

We measured the laser diameter for various distances both in the x- and the y-direction. But due to the small diameter for short distances and the very dominant diffraction pattern for larger distances, it was difficult to get accurate values only by eye. Therefore we assumed a general error of 20% on all the measurements. For the distances, we used a laser rangefinder, which is highly accurate compared to our measurements, so we consider these values to be exact.

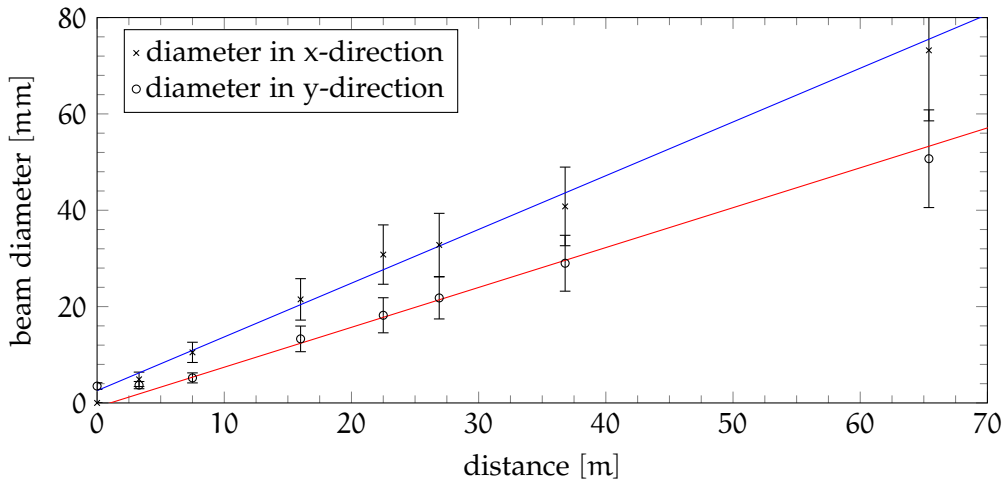


Figure 34: Measured diameters of the laser beam in x- and y-direction

Since the diameters of the laser beam is still small compared to the measured distance, a small angle approximation was used. We got the following results for the opening angle of the fit:

$$\phi_x = 0.00116(26)^\circ$$

$$\phi_y = 0.00083(16)^\circ$$

Compared to the guessed value of 0.005° , that we used in the pyOpTools and geant4 simulation ϕ_x is still 5 times smaller.

5.2 FIRST MEASUREMENTS

5.2.1 c_0 VALIDATION

Besides the opening angle of the laser, we also did a few straightforward measurements with the LIDAR itself. As mentioned previously, the final readout board was not yet available for the measurements performed during this thesis and therefore an oscilloscope has been used for the readout of the signal. The first measurements aimed at confirming basic functionality of the LIDAR and its components. The laser was aimed at a diffusely reflecting surface and the time delay between the laser trigger and the arrival of the back-scattered photons was recorded. We took the light pulse as a trigger to get information about the time difference between the shot of the pulse and the recording of the diffusely backscattered light from the wall. To get the distance to the wall, we used the same rangefinder as in the section above.

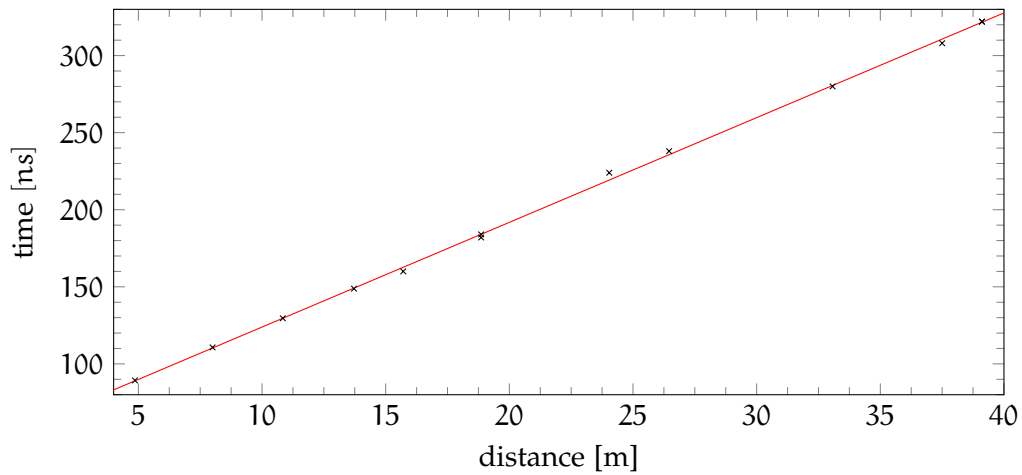


Figure 35: time delay between the shot of the beam and the detection of the backscattered light

We can retrieve the speed of light from the slope. Since the slope has units of s/m, we expect its inverse to be half of the known speed of light. Moreover, from the axes intercept, we can learn something about the general offset of the LIDAR and the oscilloscope.

$$\begin{aligned}
 t &= 2 \cdot c_{\text{meas}} \cdot x + t_{\text{offset}} \\
 2 \cdot c_{\text{meas}} &= 294\,437\,714(2176194) \text{ m/s} \\
 t_{\text{offset}} &= 55.968\,67(40) \text{ ns}
 \end{aligned}$$

Therefore the measured value for the speed of light is $0.491 \cdot c_0$. This is exactly what we expected, so the signal we saw on the oscilloscope was the return signal of the laser.

5.2.2 FIRST LIDAR MEASUREMENT

The second one was to do a first, although very primitive, LIDAR measurement. We took the data alongside the measurement described above. We triggered the oscilloscope 10000 times and always recorded when no photon was measured. This probability follows a Poisson distribution

$$P(k \text{ events}) = e^{-\lambda} \frac{\lambda^k}{k!}$$

Where k is the number of photons detected (In our case $k = 0$), $P(k \text{ events})$ the probability of detecting a photon (amounts of records divided by 10000) and λ is the expected value. It represents the expected amount of photons per trigger (the distance and the laser intensity were adjusted in a way that only in about less than 59% of the cases one or more photons were expected to reach the detector). Since the wall reflects the photons approximately isotropic, we

expect that the amount of photons per trigger follows a r^{-2} function because the surfaces of a sphere is proportional to r^{-2} .

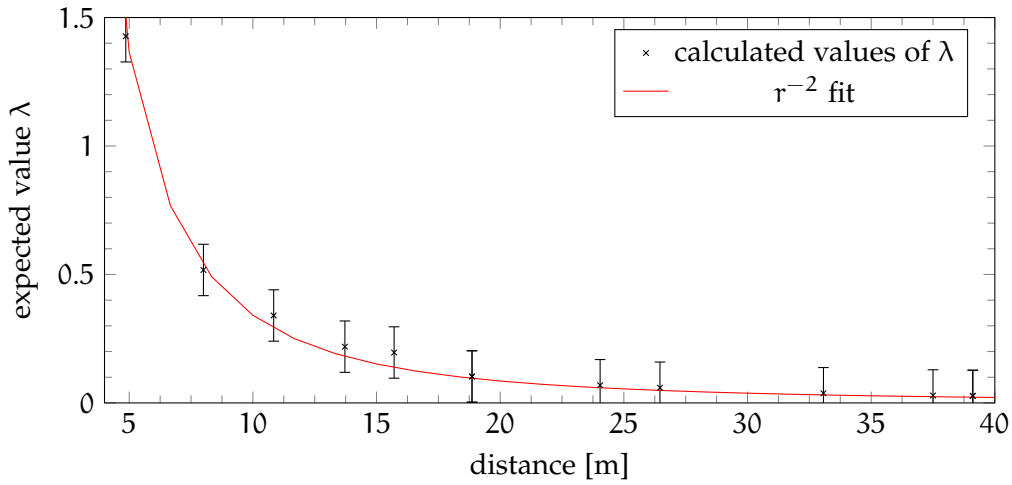


Figure 36: The expected amount of photons per trigger for various distances fitted with a r^{-2} function.

Although this is just a straightforward test and nothing was optimized at that point, we could already see the r^{-2} dependency of the signal that we are expecting. For the uncertainties, we assumed a generic value of 0.1. That follows directly from a uncertainty of 10% for $P(0)$. This was done because for reasons that could not be determined in the scope of this thesis, the oscilloscope did not always stop exactly after 10000 laser shots.

5.3 CONCLUSION AND FORESIGHT

During the work for this thesis, two simulations for the optical configuration of the LIDAR have been developed. The first one is written in pyOpTools and the second more sophisticated one in geant4, which acted as a cross-check for the first one. These simulations yielded the following values for the optics: 64 mm distance between the detector and the lens, a tilt of $6(1)^\circ$ in the vertically and $0(4)^\circ$ in the horizontally for the laser. Furthermore, a distance of 50(20) mm between the detector and the centre of the sphere and a maximum offset of 20 mm in the plane perpendicular to the optical axis have been found to give the best results. In addition to that, a third simulation has been written. It focused on the return signal of the LIDAR. When observing for 60 s, we expect to see a evaluable signal up to 150 mm. First measurements have been performed and, although very primitive, we could verify the characteristic r^{-2} dependency of the return signal.

In the upcoming months, last details for the LIDAR module will be finished, e. g. counterweights for the rotary system and more sophisticated tests will be performed. For example, performing tests in water and verify the tilt of the laser and recording long-distance signal

Part IV

APPENDIX

PYTHON CODE



```
In [1]: import numpy as np
import matplotlib.pyplot as plt
from scipy.integrate import quad
import scipy.constants as const
from scipy.interpolate import interp1d
%matplotlib inline
import mpld3
mpld3.enable_notebook()
from scipy.optimize import curve_fit
from multiprocessing.dummy import Pool
import itertools
from time import time
```

Backgroundnoise

```
In [2]: #Runterrechnung auf PMT
f_ges = 10**6/(2*np.pi*100*np.pi)*2.5**2*np.pi/63**2*3
```

```
In [3]: mu, sigma = 450, 150 # mean and standard deviation
width = 500
s = np.random.normal(mu, sigma, 1000000)
count, bins, ignored = plt.hist(s, bins = width, density = True)
func = []
for i in bins:
    x = 1/(sigma*np.sqrt(2*np.pi))*np.exp(-(i-mu)**2/(2 * sigma**2))
    func.append(x)
plt.plot(bins, func,
         linewidth=2, color='r')
plt.show()
```

PMT

```
In [4]: Werte = [0.014, 0.1126, 0.17, 0.171, 0.17878, 0.14,
0.1033, 0.06, 0.04, 0.01424, 0.0013, 3.405*10**(-5)]
xp = [270, 300, 325, 350, 400, 450, 500, 525, 550, 600, 650, 700]
xvals = np.linspace(300, 700, width)
yinterp = np.interp(xvals, xp, Werte)

f = []
for i in range(width):
    f.append(yinterp[i]*func[i])
```

Final Noise PMT

```
In [5]: noise = np.zeros(len(f))
for i in range(len(f)):
    noise[i] = f[i]
noise_detector = 0
noise_detec = [] #
xvalues = [] #Wellenlngen, die f r den Detektor relevant sind
for i in range(len(f)):
    if xvals[i] > 445 and xvals[i] < 455:
        noise_detector += noise[i]
        noise_detec.append(noise[i])
        xvalues.append(xvals[i])

noise_ges = np.trapz(noise)
ratio = noise_detector/noise_ges
noise_final = f_ges * ratio + 1
noise_N = (noise_final) * 20*10**(-9)
```

Photonnumber

```
In [6]: N_0 = 10**9 #Photonen pro Laserpuls
scat = 300. #Streulnge von Wasser
att = 30. #attenuation length in water von Wasser
freq =50000#*30*5 #frequenz des Lasers x Messzeit
n = 111
beta = 0.011
sigma = 1./att
L = 250.
dr = float(L)/n #length that light travels in water in 20ns
    (always back and forth!)

C = 0.1 #Effizienz
A = 0.0105**2*np.pi #Effektive Fl che in m, Filter
rate = np.zeros(n) #Anzahl an Photonen f r jeden Schritt
length = np.zeros(n) #die Abst nde nach jedem Schritt
rate_Hz = np.zeros(n) #Anzahl der Photonen pro Sekunde
for i in range(n):
    r = dr*i+2.36
    integrand = quad(lambda x:sigma, 0, r)
    N_i = C*N_0*A/(r**2)*beta*dr*np.exp(-2*integrand[0])
    length[i] = r
    rate[i] = N_i
    rate_Hz[i] = rate[i]/(20*10**(-9))
```

```
In [7]: for i in range(len(length)):
        if rate_Hz[i] >= 50*10**6*freq:
            pass
        else:
            l_min = length[i]
            i_min = i
            print "Minimaler Abstand:", l_min
            break
    for i in range(len(length)):
        if rate_Hz[i] >(noise_final)+freq:
            pass
        else:
            print "Maximaler Abstand:", length[i]
            break

    #Umrechnung der Länge in Zeit
    time = np.zeros(n)
    dt = 2*dr*1.33/const.c
    for i in range(len(length)):
        time [i] = length[i]*2*1.33/const.c

    plt.plot(length, rate_Hz, "B")
    plt.yscale("log")
    plt.show()
```

Background Simulation

```
In [8]: backg = np.zeros(len(length))
        backg_photons = noise_final*freq*length[-1]*2*1.33/const.c
        print backg_photons
        backg = np.random.uniform(0,length[-1], int(backg_photons))
        backg_photons, bins, ignored = plt.hist(backg, bins = length)
        plt.show()
```

Final Return Signal Simulation

```
In [9]: N_ges = np.zeros(n+1)
        l2 = np.zeros(n+1)
        for i in range(n):
            N_ges[i+1] = N_ges[i] + rate[i]
            l2[i] = dr*i+2.36
        l2[n] = dr*(n+1)+2.36

        rand = np.random.random(int(N_ges[-1]))
        N_max = N_ges[-1]
        N_ges /= N_max

        #interpolieren
        interp = interp1d(N_ges, l2)

        plt.hist(interp(rand), bins = length)
        plt.show()
```

```

In [10]: detected = []
def photon_sim():
    rand = np.random.random(int(N_max))
    photons = interp(rand)
    photons = photons*2*1.33/const.c
    photons = np.sort(photons)
    counted = [photons[0]]
    for j in range(len(photons)):
        if (counted[-1] + dt) > photons[j]:
            pass
        else:
            counted.append(photons[j])
    return counted

for i in range(freq):
    a = photon_sim()
    detected.extend(a)

length2 = np.zeros(111)
for i in range(111):
    r = dr*100*i+2.36
    length2[i] = r

detected = np.array(detected)*const.c/(2*1.33)

detec_photons, bins, ignored = plt.hist(detected, bins = length )

bins = bins[:-1]
ende = time()
detec_photons += backg_photons

plt.plot(bins, np.array(detec_photons)*bins**2)
plt.yscale('log')
plt.show()

```

BIBLIOGRAPHY

- [1] BK-7 Glass | Optical Borosilicate Crown Glass Manufacturer. URL: <http://www.zcq-quartz.com/glass-2.html> (visited on 07/06/2019).
- [2] A. Bernstein, Y. Wang, G. Gratta, and T. West. “Nuclear reactor safeguards and monitoring with antineutrino detectors.” In: *Journal of Applied Physics* 91.7 (Apr. 2002), pp. 4672–4676. ISSN: 0021-8979, 1089-7550. DOI: [10.1063/1.1452775](https://doi.org/10.1063/1.1452775). URL: <http://aip.scitation.org/doi/10.1063/1.1452775> (visited on 07/21/2019).
- [3] J. Billard, L. Strigari, and E. Figueroa-Feliciano. “Implication of neutrino backgrounds on the reach of next generation dark matter direct detection experiments.” In: *Physical Review D* 89.2 (Jan. 27, 2014), p. 023524. ISSN: 1550-7998, 1550-2368. DOI: [10.1103/PhysRevD.89.023524](https://doi.org/10.1103/PhysRevD.89.023524). arXiv: [1307.5458](https://arxiv.org/abs/1307.5458). URL: <http://arxiv.org/abs/1307.5458> (visited on 07/21/2019).
- [4] M. Boehmer et al. “STRAW (STRings for Absorption length in Water): pathfinder for a neutrino telescope in the deep Pacific Ocean.” In: *Journal of Instrumentation* 14.2 (Feb. 13, 2019), P02013–P02013. ISSN: 1748-0221. DOI: [10.1088/1748-0221/14/02/P02013](https://doi.org/10.1088/1748-0221/14/02/P02013). arXiv: [1810.13265](https://arxiv.org/abs/1810.13265). URL: <http://arxiv.org/abs/1810.13265> (visited on 07/18/2019).
- [5] CERN experiments observe particle consistent with long-sought Higgs boson. CERN. URL: <https://home.cern/news/press-release/cern/cern-experiments-observe-particle-consistent-long-sought-higgs-boson> (visited on 07/21/2019).
- [6] T. Chiarusi and M. Spurio. “High-energy astrophysics with neutrino telescopes.” In: *The European Physical Journal C* 65.3 (Feb. 1, 2010), pp. 649–701. ISSN: 1434-6052. DOI: [10.1140/epjc/s10052-009-1230-9](https://doi.org/10.1140/epjc/s10052-009-1230-9). URL: <https://doi.org/10.1140/epjc/s10052-009-1230-9> (visited on 07/22/2019).
- [7] IceCube Collaboration. “Neutrino emission from the direction of the blazar TXS 0506+056 prior to the IceCube-170922A alert.” In: *Science* (July 12, 2018), eaat2890. ISSN: 0036-8075, 1095-9203. DOI: [10.1126/science.aat2890](https://doi.org/10.1126/science.aat2890). arXiv: [1807.08794](https://arxiv.org/abs/1807.08794). URL: <http://arxiv.org/abs/1807.08794> (visited on 07/20/2019).
- [8] IceCube Collaboration et al. “The IceCube Neutrino Observatory: Instrumentation and Online Systems.” In: *Journal of Instrumentation* 12.3 (Mar. 14, 2017), P03012–P03012. ISSN: 1748-0221. DOI: [10.1088/1748-0221/12/03/P03012](https://doi.org/10.1088/1748-0221/12/03/P03012). arXiv: [1612.05093](https://arxiv.org/abs/1612.05093). URL: <http://arxiv.org/abs/1612.05093> (visited on 07/20/2019).

- [9] SNO Collaboration. “Measurement of the rate of $\nu_e + d \rightarrow p + p + e^-$ interactions produced by 8B solar neutrinos at the Sudbury Neutrino Observatory.” In: *Physical Review Letters* 87.7 (July 25, 2001), p. 071301. ISSN: 0031-9007, 1079-7114. DOI: [10.1103/PhysRevLett.87.071301](https://doi.org/10.1103/PhysRevLett.87.071301). arXiv: [nucl - ex / 0106015](https://arxiv.org/abs/nucl-ex/0106015). URL: <http://arxiv.org/abs/nucl-ex/0106015> (visited on 07/21/2019).
- [10] The IceCube Collaboration. “The Design and Performance of IceCube DeepCore.” In: *Astroparticle Physics* 35.10 (May 2012), pp. 615–624. ISSN: 09276505. DOI: [10.1016/j.astropartphys.2012.01.004](https://doi.org/10.1016/j.astropartphys.2012.01.004). arXiv: [1109.6096](https://arxiv.org/abs/1109.6096). URL: <http://arxiv.org/abs/1109.6096> (visited on 07/20/2019).
- [11] Raymond Davis. “Solar Neutrinos. II. Experimental.” In: *Physical Review Letters* 12.11 (Mar. 16, 1964), pp. 303–305. ISSN: 0031-9007. DOI: [10.1103/PhysRevLett.12.303](https://doi.org/10.1103/PhysRevLett.12.303). URL: <https://link.aps.org/doi/10.1103/PhysRevLett.12.303> (visited on 07/21/2019).
- [12] *Differential Absorption Lidar - an overview | ScienceDirect Topics*. URL: <https://www.sciencedirect.com/topics/earth-and-planetary-sciences/differential-absorption-lidar> (visited on 05/13/2019).
- [13] *Figure 2.8: Schematic view of an air shower with separated hadronic,...* URL: https://www.researchgate.net/figure/Schematic-view-of-an-air-shower-with-separated-hadronic-muonic-and-electromagnetic_fig5_41217371 (visited on 07/21/2019).
- [14] Christian Fruck. *A new LIDAR system for the MAGIC telescopes and site search instrumentation for CTA*. 2011. URL: https://magicold.mpp.mpg.de/publications/theses/CFruck_diploma.pdf (visited on 05/07/2019).
- [15] Carlo Giunti and Chung W. Kim. *Fundamentals of Neutrino Physics and Astrophysics*. Oxford University Press, Mar. 15, 2007. ISBN: 978-0-19-170886-2. URL: <https://www.oxfordscholarship.com/view/10.1093/acprof:oso/9780198508717.001.0001/acprof-9780198508717> (visited on 07/21/2019).
- [16] Hamamatsu. *H12406 PMT*. URL: https://www.hamamatsu.com/resources/pdf/etd/MicroPMT_TPMZ1019E.pdf (visited on 07/15/2019).
- [17] *Micro PMT photon counting head H12406*. URL: <https://www.hamamatsu.com/eu/en/product/type/H12406/index.html> (visited on 07/13/2019).
- [18] Gustav (Physiker) Mie. *Beiträge zur Optik trüber Medien, speziell kolloidaler Metallösungen*. Google-Books-ID: nuzqcQAACAAJ. 1908. 68 pp.
- [19] P. Padovani, P. Giommi, E. Resconi, T. Glauch, B. Arsioli, N. Sahakyan, and M. Huber. “Dissecting the region around IceCube-170922A: the blazar TXS 0506+056 as the first cosmic neutrino source.” In: *Monthly Notices of the Royal Astronomical Society* 480.1 (Oct. 11, 2018), pp. 192–203. ISSN: 0035-8711, 1365-2966. DOI: [10.1093/mnras/sty1852](https://doi.org/10.1093/mnras/sty1852). arXiv: [1807.04461](https://arxiv.org/abs/1807.04461). URL: <http://arxiv.org/abs/1807.04461> (visited on 07/20/2019).
- [20] M. Salaris and S. Cassisi. *Evolution of Stars and Stellar Populations*. Wiley, 2005. ISBN: 978-0-470-09222-4.

- [21] Sellmeier. "Zur Erklärung der abnormen Farbenfolge im Spectrum einiger Substanzen." In: *Annalen der Physik* 219.6 (1871), pp. 272–282. ISSN: 1521-3889. DOI: [10.1002/andp.18712190612](https://doi.org/10.1002/andp.18712190612). URL: <https://onlinelibrary.wiley.com/doi/abs/10.1002/andp.18712190612> (visited on 07/06/2019).
- [22] Thorlabs. *FBH450-10 - Premium Bandpass Filter, Ø25 mm, CWL = 450 nm, FWHM = 10 nm*. URL: <https://www.thorlabs.com/thorproduct.cfm?partnumber=FBH450-10> (visited on 06/02/2019).
- [23] Thorlabs. *LA1134-A N-BK7 Plano-Convex Lens, Ø1", f = 60.0 mm, AR Coating: 350-700 nm*. URL: <https://www.thorlabs.com/thorproduct.cfm?partnumber=LA1134-A> (visited on 06/02/2019).
- [24] Thorlabs. *Laser Manual*. URL: <https://www.thorlabs.com/drawings/642bce8d8d8d58df-5B66E420-D4B1-BA2E-5502B6497052FFA1/NPL45B-Manual.pdf> (visited on 07/14/2019).
- [25] Thorlabs. *Laser NPL45B*. URL: https://www.thorlabs.com/newgrouppage9.cfm?objectgroup_id=10823#ad-image-0 (visited on 07/15/2019).
- [26] Thorlabs. *Tutorials*. URL: <https://www.thorlabs.com/tutorials.cfm?tabID=4BD528B8-11B1-4D32-BE81-CB0C6EBF020C> (visited on 07/12/2019).
- [27] Thorlabs. *Tutorials*. URL: <https://www.thorlabs.com/tutorials.cfm?tabID=F7ED0DD5-3F31-4F84-9843-E0F7AC33F413> (visited on 07/11/2019).
- [28] Claus Weitkamp. *Lidar: Range-Resolved Optical Remote Sensing of the Atmosphere*. Google-Books-ID: QWzrBwAAQBAJ. Springer Science & Business, June 3, 2006. 467 pp. ISBN: 978-0-387-25101-1.
- [29] *schott-datasheet-n-bk7.pdf*. URL: https://www.schott.com/advanced_optics/german/abbe_datasheets/schott-datasheet-n-bk7.pdf (visited on 06/02/2019).

ACKNOWLEDGEMENTS

These lines are dedicated to all the people who supported me in the course of this thesis. First i would like to thank Prof. Elisa Resconi for giving me the opportunity to be a part of this amazing group. Secondly many thanks goes to my supervisor Dr. Christian Fruck and his large expertise and guidance. His great advice and ideas gave rise to many interesting topics of this thesis. A special thanks goes to Kilian Holzapfel. He provided the basis for my own geant4 simulation. Without his simulation i would have potentially not been able to finish my own. I also want to thank the rest of the members of the group for many discussions, conversations and the exceptional atmosphere in this group. And lastly i would like to thank my family, friends and my girlfriend who supported and encouraged me throughout the whole thesis.